CELL BIOLOGY

Platelets drive fibronectin fibrillogenesis using integrin αIIbβ3

Sebastian Lickert[1], Martin Kenny[2], Kateryna Selcuk[1], Johanna L. Mehl[1], Markus Bender[3], Susanna M. Früh[4,5], Melanie A. Burkhardt[1], Jan-Dirk Studt[6], Bernhard Nieswandt[3], Ingmar Schoen[2]*†, Viola Vogel[1]*†

Platelets interact with multiple adhesion proteins during thrombogenesis, yet little is known about their ability to assemble fibronectin matrix. In vitro three-dimensional superresolution microscopy complemented by biophysical and biochemical methods revealed fundamental insights into how platelet contractility drives fibronectin fibrillogenesis. Platelets adhering to thrombus proteins (fibronectin and fibrin) versus basement membrane components (laminin and collagen IV) pull fibronectin fibrils along their apical membrane versus underneath their basal membrane, respectively. In contrast to other cell types, platelets assemble fibronectin nanofibrils using αIIbβ3 rather than α5β1 integrins. Apical fibrillogenesis correlated with a stronger activation of integrin-linked kinase, higher platelet traction forces, and a larger tension in fibrillar-like adhesions compared to basal fibrillogenesis. Our findings have potential implications for how mechanical thrombus integrity might be maintained during remodeling and vascular repair.

INTRODUCTION

When blood vessels get injured, the massive recruitment and activation of platelets culminate in thrombus formation to stop bleeding, whereas the subsequent infiltration of the clot by immune and stromal cells ultimately restores tissue integrity (*1*). Defects in platelet constituents that mediate platelet anchorage and contractility (adhesion receptors, actin cytoskeleton, and myosin IIa) result in compromised thrombus stability, frequent embolization, and increased (re-)bleeding (*2*–*4*). In particular, the platelet integrin αIIbβ3 plays an unmatched role in platelet biomechanics because it mediates stable adhesion at injury sites, platelet-platelet aggregation, as well as migration (*5*). Maintaining the mechanical stability of the clot and its physical connection to the surrounding tissue during remodeling is important for successful wound healing. The formation of fibronectin (Fn) matrix by invading fibroblasts is a hallmark of wound healing (*1*). In vascular development and in tissue repair, Fn matrix provides an essential scaffold to guide cell migration and to instruct the deposition of mature extracellular matrix (ECM) (*6*, *7*). Plasma Fn (pFn) has been reported to contribute to hemostasis and affect thrombus structure (*8*), but it is not known whether Fn is present in the clot in its fibrillar form nor whether platelets are the first cells to assemble the first provisional Fn matrix.

The mechanisms underlying cell-driven Fn fibrillogenesis have been extensively studied in fibroblasts (*9*). Fn fibrils are formed at fibrillar adhesions that couple the ends of Fn fibrils to the contractile actin cytoskeleton. Fibrillar adhesions in fibroblasts are enriched in α5β1 integrins and tensin and low in phospho-tyrosine (PY). While "classical" three-dimensional (3D)–like fibrillar adhesions are formed by the back-translocation of α5β1 along actin stress fibers at the apical membrane of fibroblasts cultured on Fn (*9*), a recent study described a distinct type of "sliding" fibrillar adhesion formed by the segregation of α5β1 integrins from focal adhesions in the basal membrane of fibroblasts on basement membrane proteins (*10*). This latter phenomenon shares similarities with the basal 2D deposition of Fn fibrils by endothelial cells, which proceeds in the absence of stress fibers (*11*, *12*). The determining factors of 3D versus 2D Fn fibrillogenesis in fibroblasts are unclear, and the definition of fibrillar adhesions and their formation mechanisms is thus still being refined.

Whether platelets not only secrete ECM proteins but also assemble the first provisional Fn matrix is controversial. Platelet-deposited Fn is deoxycholate-insoluble (*13*, *14*), which suggests that it exists in its fibrillar form. While several different ECM protein coatings support Fn deposition by platelets, including Fn and fibrin (Fb) (*13*), laminin (Ln) (*14*), or collagen type I (*15*), others such as vitronectin or fibrinogen (Fg) (*16*) or von Willebrand factor (*15*) do not. Whether the different observed deposition patterns on different adhesion proteins use different mechanisms for apical or basal assembly, as in fibroblasts, is not known. The spatial resolution of confocal microscopy cannot resolve the dimensions of Fn fibrils, while few electron microscopy data suggest that fibrils might be as thin as 20 nm (*13*). αIIbβ3 is the only integrin besides α5β1 that has a synergy site known to reinforce cell adhesion (*17*) and thought to be important for Fn fibrillogenesis (*9*). Specific inhibitors against the two Fn-binding integrins in platelets, αIIbβ3 or α5β1, reduced Fn deposition on Fn or Fb substrates to different degrees (*13*), but it remained unclear whether this reduction was due to reduced platelet-substrate adhesion or to reduced Fn fibrillogenesis. Since αIIbβ3 is exclusively expressed in the megakaryocytic lineage, its potential to assemble Fn fibrils and the molecular machinery and mechanisms coordinating Fn fibrillogenesis in platelets remain largely unknown.

[1]Laboratory of Applied Mechanobiology, Department of Health Sciences and Technology, ETH Zurich, Vladimir-Prelog-Weg 4, 8093 Zurich, Switzerland. [2]Irish Centre for Vascular Biology, School of Pharmacy and Biomolecular Sciences, Royal College of Surgeons in Ireland, 123 St Stephen's Green, Dublin 2, Ireland. [3]Institute of Experimental Biomedicine – Chair I, University Hospital, and Rudolf Virchow Center, Julius Maximilian University of Würzburg, Josef-Schneider-Str. 2, 97080 Würzburg, Germany. [4]Hahn-Schickard, Georges-Koehler-Allee 103, 79110 Freiburg, Germany. [5]Laboratory for MEMS Applications, IMTEK Department of Microsystems Engineering, University of Freiburg, Georges-Koehler-Allee 103, 79110 Freiburg, Germany. [6]Division of Hematology, University Hospital Zurich, Rämistrasse 100, 8091 Zurich, Switzerland.
*Corresponding author. Email: viola.vogel@hest.ethz.ch (V.V.); ingmarschoen@rcsi.ie (I.S.)
†These authors contributed equally to this work.

This study investigates the mechanobiological mechanisms of Fn fibrillogenesis by human platelets adhering via integrins to different ECM protein coatings. 3D direct stochastic optical reconstruction microscopy (3D STORM) was exploited to resolve nanoscale Fn fibrils at platelet-matrix adhesion sites and to distinguish between basal and apical ECM assembly, complemented by micropost arrays for correlative platelet traction force measurements. Platelets, like other cells, form highly elongated fibrillar-like adhesion morphologies as they assemble Fn nanofibrils but display notable differences in their composition compared to fibroblasts, especially as they drive Fn fibrillogenesis via αIIbβ3 instead of α5β1 integrins, as found here. Platelets assembled two distinct Fn matrix architectures and developed different contractility on surfaces coated with either blood clot or basement membrane proteins. These findings point to so far unrecognized mechanisms how platelets can actually sense their microenvironment and respond to it by adjusting their contractility and the local Fn matrix deposition pattern. Our findings also challenge the common notion that infiltrating fibroblasts or mesenchymal stem cells are the first cells to assemble a de novo Fn ECM at wound sites (*9*, *18*).

RESULTS

Substrate adherent platelets assemble Fn nanofibrils

Since confocal microscopy falls short to characterize platelet-assembled Fn fibrils (*13*, *14*), we used superresolution microscopy (3D STORM) to analyze washed human platelets on Fn-coated glass and supplemented the medium with fluorescently labeled human pFn that is harvested by cells for fibrillogenesis (Fig. 1A). Three distinct localizations of labeled Fn were observed in platelets spread on Fn after 2 hours (Fig. 1B and fig. S1A). (i) Short stubby Fn deposits were arranged perpendicular to the cell edge periphery (Fig. 1C). (ii) Longer Fn fibrils were formed mainly at opposite ends of platelets and spanned from the outside of the cell further into the cell (Fig. 1D). (iii) Punctate aggregated Fn signals were found more centrally but exclusively on top of the cell (red color code in Fig. 1B). The longer Fn fibrils and the Fn aggregates were seen to be aligned to and located along pronounced filamentous (F-)actin bundles (gray epifluorescence overlay in Fig. 1, B to D) which spanned the cell in a characteristic "bipolar" arrangement as described previously (*19*).

Since platelets bind to different ECM proteins after vascular injury, we asked whether the spatial architecture of de novo assembled Fn fibrils depends on the ECM proteins to which the platelets adhere. In platelets spread on the basement membrane protein Ln-111, the arrangement of deposited labeled Fn was notably different and showed two main features (Fig. 1E). (i) Pronounced Fn fibrils were pointing from the peripheral actin ring radially inward toward the pronounced ring-shaped central actin bundle (Fig. 1F), in agreement with previously reported Fn deposition patterns (*14*) and cytoskeletal arrangements (*19*). (ii) Punctuate aggregated Fn signals were found centrally and exclusively beneath the platelet (blue-cyan color code in Fig. 1E).

Fibrils shorter than 1 μm were difficult to distinguish unambiguously from aggregates and were thus not investigated quantitatively. A statistical analysis of longer fibrils revealed that platelets from different normal healthy donors assembled fibrils with consistent characteristic dimensions (figs. S1 and S2). Fibrils were up to 4 μm long and had a similar length on Fn (1.7 ± 0.5 μm) compared to Ln coatings (1.8 ± 0.6 μm; means ± SD; Fig. 1G). The diameter of most fibrils ranged from 20 to 250 nm, while fibrils on Ln appeared thicker (119 ± 79 nm) than on Fn (90 ± 47 nm; $P < 10^{-6}$; Fig. 1H), which might be related to their curvier appearance on Ln (Fig. 1F), indicating that they are under less tension.

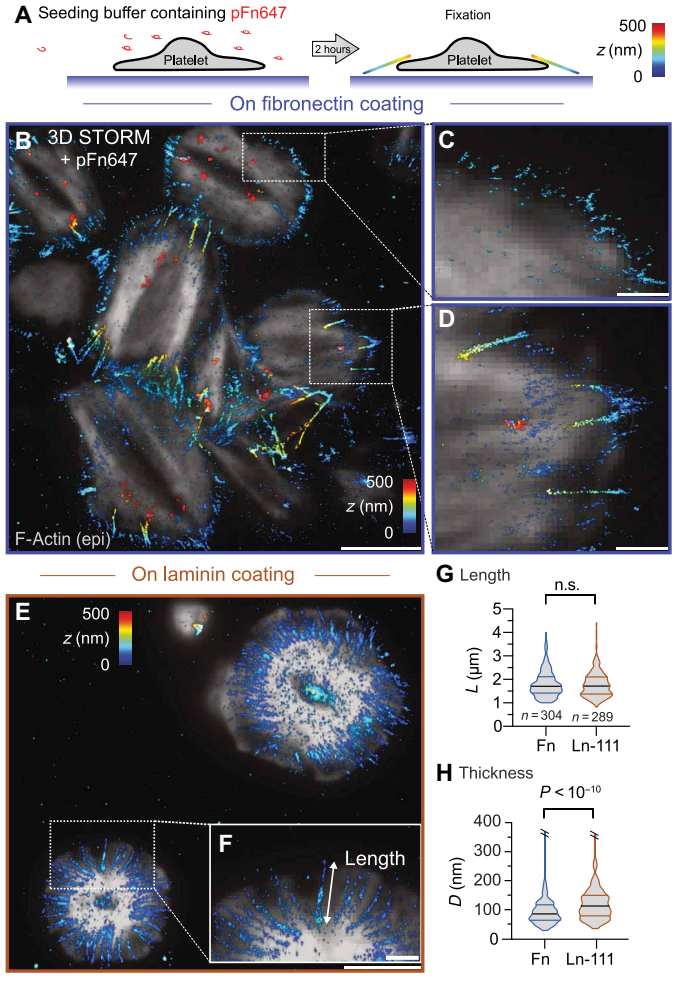

Fig. 1. Fn extracellular matrix assembled by human platelets on Fn-coated and Ln-111–coated coverslips. (**A**) Sketch of the experimental procedure. Platelets are seeded on Fn-coated or Ln-coated glass coverslips for 2 hours at 37°C in a medium supplemented with pFn (90 μg ml^{-1}) and pFn647 (10 μg ml^{-1}). During this time, platelets incorporate labeled pFn into newly assembled Fn fibers. Samples are then fixed and imaged by superresolution microscopy. (**B**) 3D STORM of pFn647 assembled by platelets on Fn-coated glass coverslips. The *z* position of pFn647 is color-coded from blue (basal) to red (apical). All STORM images are overlaid onto an epifluorescence (epi) image of F-actin (gray). (**C**) Magnified view of pFn fibrils at the cell periphery showing submicrometer-long Fn deposits. (**D**) Magnified view of pFn fibrils at the cell end showing micrometer-long Fn fibrils. (**E**) 3D STORM of Fn647 assembled by platelets on Ln-111–coated glass coverslips. (**F**) Magnified view of radially oriented micrometer-long Fn fibrils. (**G**) Length *L* and (**H**) thickness *D* of pFn fibrils extracted from 3D STORM data of fibrils formed on Fn versus Ln-111 coatings. Data distributions are depicted as violin plots showing the median (thick black line) and interquartile ranges (thin colored lines). Data were compared with an unpaired two-tailed Mann-Whitney test. Adjusted $P < 0.001$ was accepted as highly significant. n.s., not significant. Data were pooled from nine donors (24 to 35 years). Only fibrils longer than 1 μm were included in the analysis. Scale bars, 5 μm (B and E) and 1 μm (C, D, and F).

Fn fibril assembly follows the time-dependent remodeling of the actin cytoskeleton within minutes

To better understand whether the two Fn deposition patterns on Ln and Fn follow distinct formation mechanisms or are merely different temporal stages of the same assembly process, we characterized the temporal deposition sequence of fibrils up to fixation time points at 15, 30, 45, and 120 min. Figure 2 shows representative platelets for each time point. On Fn, fibrils appeared at the earliest investigated time point and were aligned flat with actin bundles of former filopodia (Fig. 2A and fig. S3A). Over the subsequent 30 min, short Fn fibrils

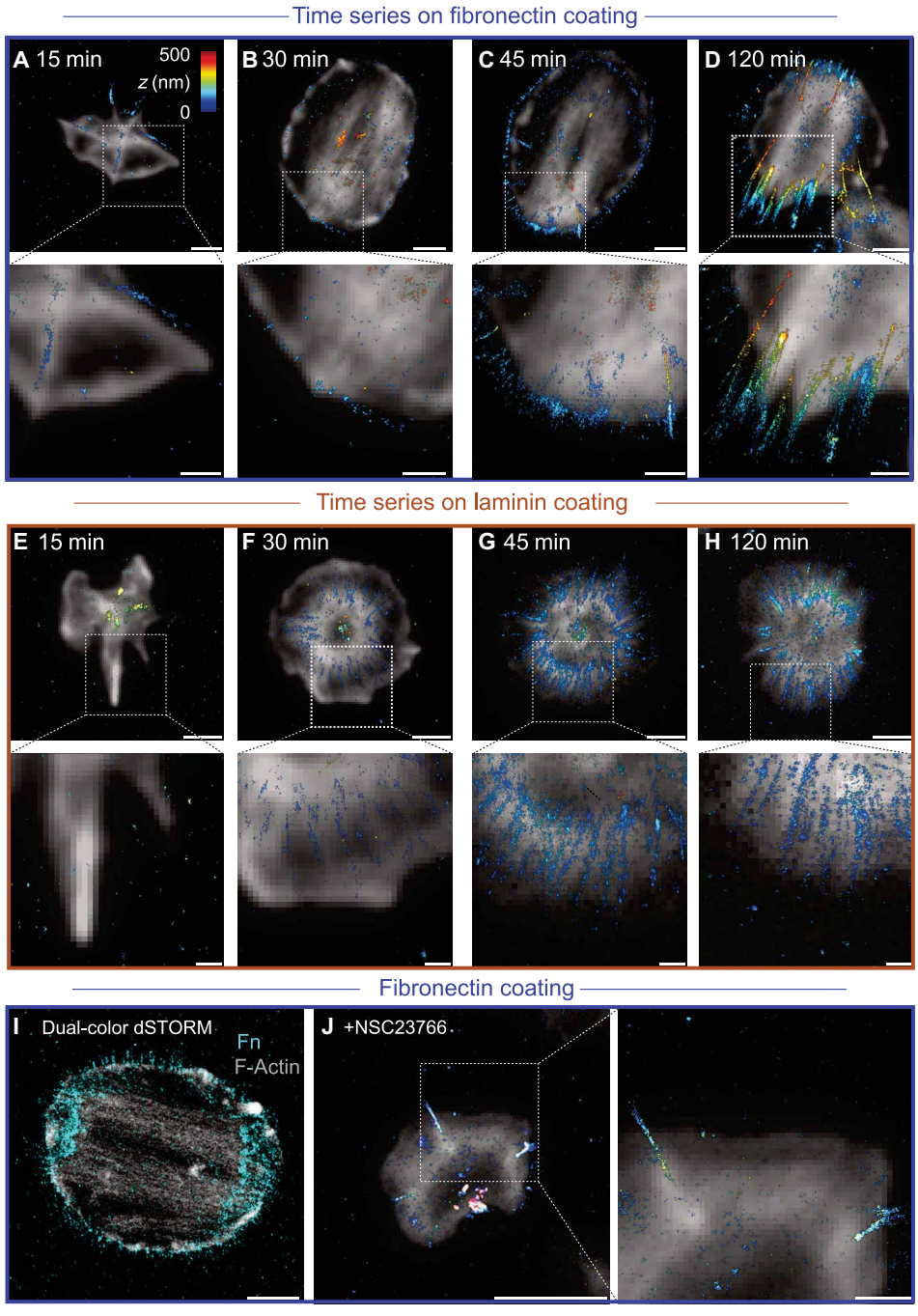

Fig. 2. Temporal sequence of Fn fibril assembly by platelets and dependence on lamellipodia dynamics. (**A** to **D**) 3D STORM of pFn647 assembled by platelets on Fn-coated glass coverslips after 15 (A), 30 (B), 45 (C), and 120 min (D). Shown are representative platelets for each time point. The *z* position of pFn647 is color-coded from blue (basal) to red (apical). All STORM images are overlaid onto an epifluorescence (epi) image of F-actin (gray). Bottom row: Magnified views of the boxed regions. (**E** to **H**) pFn647 assembled by platelets on Ln-coated glass coverslips after 15 (E), 30 (F), 45 (G), and 120 min (H). Bottom row: Magnified views of the boxed regions. (**I**) pFn647 assembled on Fn-coatings by platelets treated with 100 μM change to Rac-1 selective inhibitor NSC23766. Right: Magnified view. (**J**) Representative dual-color STORM image of pFn680 (cyan) and phalloidin-647 (gray) in a single platelet seeded for 120 min on Fn-coated glass. Platelets were obtained from three donors (24 to 34 years). Scale bars, 5 μm (I), 2 μm (A to H, top rows, and J), and 1 μm (A to I, magnified views).

were formed at the cell edge perpendicular to the peripheral actin ring, while the main F-actin bundles adopted their characteristic bipolar arrangement (Fig. 2, B and C, and fig. S3, B and C). From the 45-min time point onward, an increasing number of Fn fibrils anchored at the two ends of the main F-actin bundles (Fig. 2D and fig. S3D). On Ln, hardly any fibrils were observed at the earliest time point (Fig. 2E and fig. S4A). Most radial fibrils formed between 15 and 45 min (Fig. 2, F and G, and fig. S4, B and C). Their arrangement remained stable up to the longest investigated time point (Fig. 2H and fig. S4D). In summary, most long fibrils on Fn coatings formed only after platelets had adopted a stable F-actin cytoskeleton and were thus seen at later time points compared to those on Ln coatings.

As Fn fibrillogenesis is initiated by actomyosin tensile forces that partially expose cryptic Fn-Fn assembly sites (*9*), and as an impaired cytoskeleton reduces Fn deposition by platelets (*14*) and by other cells (*20*), we next analyzed the spatial organization of the actin cytoskeleton with respect to the formed fibrils using dual-color STORM. The majority of platelets on Fn coatings formed a highly aligned bipolar F-actin network with pronounced bundles traversing the cell. Longer Fn fibrils emanated parallel to these actin cables at adhesion sites situated at both ends and extended beyond the platelet edge (Fig. 2I).

Recent platelet studies have shown that lamellipodia formation is dispensable for hemostasis (*21*) but is required for platelet haptotaxis (*5*). We thus asked whether lamellipodia might play a particular role in platelet-driven Fn fibrillogenesis on Fn. While the inhibition of lamellipodia dynamics by blocking Rac-1 using NSC23766 (100 μM) abolished the formation of short Fn fibrils at the cell edge, it caused only a minor reduction in the number of longer fibrils and no change in their arrangement, as well as a notable increase of centrally located Fn deposits on top of spread platelets (Fig. 2J, magnified view, and fig. S5, A to D). Similar effects were observed upon inhibition of filopodia formation by blocking Cdc-42 using ML141 (100 μM), which also reduces lamellipodia dynamics (fig. S5, E to H). These results indicate a role for branched actin dynamics in the formation of peripheral stubby Fn fibrils but not for the assembly of longer Fn fibrils, which are associated with major F-actin bundles.

These time series and inhibitor experiments thus showed that Fn fibril assembly followed the reorganization of the F-actin cytoskeleton into stable, contractile arrangements that were not interconvertible between different adhesion protein coatings.

Fn fibrils are mostly pulled along the apical versus basal side of the platelet membrane on Fn versus Ln coatings

3D STORM provides precise *z* information and thus allows us to interrogate whether fibril-forming adhesions are located on the basal or apical side of platelets. On Fn coatings, fibrils were anchored outside of the platelet at the coverslip surface and stretched straight upward over the platelet, which is apparent from the *z* color code which ranges from blue to red or from the *x*-*z* side view (Fig. 3A and fig. S6A). The start-to-end height difference of fibrils formed by Fn-adherent platelets was 246 ± 126 nm (Fig. 3C). In direct comparison, fibroblasts produced longer and thicker Fn fibers due to profilament bundling (*9*) but showed the same start-to-end height (fig. S7). To validate an apical versus basal Fn fibril membrane attachment, we measured the height of the lamellipodium by imaging the peripheral F-actin rim at the cell edge and obtained 190 ± 37 nm (Fig. 3D and fig. S8). With more than 75% of Fn fibrils having a start-to-end height greater than 190 nm, we conclude that the majority of Fn fibrils formed on Fn were connected to the apical platelet membrane, similar to fibrillar adhesions in fibroblasts.

In contrast, platelets on Ln assembled Fn fibrils at their basal membrane, i.e., between the platelets and the coverslip, as apparent from a uniform blue color code or from the *x*-*z* side view (Fig. 3B, Movie S1, and fig. S6B). Fibril start-to-end height (90 ± 77 nm, $P < 10^{-15}$) was significantly decreased (Fig. 3C). No statistically significant differences were found for the tested Ln isoforms 111 or 411 (fig. S9). Only ~10% of fibrils formed on Ln coatings were higher than the lamellipodium, with the majority being anchored at the basal side.

To further validate the basal versus apical membrane anchorage of fibrils, we performed dual-color 3D STORM imaging with vinculin as an intracellular adhesion site marker. While the *z* resolution of ~30 nm achieved by the astigmatic 3D STORM was not sufficient to clearly discern *z* layers of different vinculin localization at adhesions as resolved by interferometric photo-activated localisation microscopy (iPALM) (*22*), our measurements confirmed that the average localization of vinculin was below Fn fibrils for platelets on Fn (Fig. 3E) and around/above Fn fibrils for platelets on Ln (Fig. 3F), as expected for fibrils being anchored at apical and basal adhesions, respectively. To differentiate between these two distinct Fn fibril architectures, we will refer to them as 3D (on Fn) and 2D (on Ln).

Fn fibrillogenesis in platelets is mostly driven by αIIbβ3 integrins, not α5β1 integrins

Since α5β1 integrins drive Fn fibrillogenesis in mesenchymal cells, yet the platelet integrin αIIbβ3 recognizes Fn's synergy site too (*23*), we next asked which integrin was driving Fn fibrillogenesis. Both integrins are expressed at very different levels, with α5β1 counts being only ~3% compared to αIIbβ3 (*24*, *25*). Since inhibition of αIIbβ3 or α5β1 would also interfere with the anchorage to Fn coatings, we conducted the experiments on Ln where platelets adhere independently via α6β1 (Fig. 4A). Blocking αIIbβ3 integrins by the nonpriming inhibitor RUC-2 (100 μM) completely abolished Fn fibril formation (Fig. 4B). In contrast, blocking α5β1 by the antibody JBS5 (20 μg ml^{-1}; Fig. 4C) showed no differences to the control with regard to fibril length or the fraction of platelets which assembled Fn fibrils (Fig. 4, D and E). Note that neither inhibitor affected platelet adhesion and spreading on Ln (fig. S10A). In contrast, Fn assembly by fibroblasts was markedly reduced with JBS5 treatment, whereas RUC-2 treatment had no effect (fig. S10B). Integrin αIIb-deficient (*Itga2b*$^{-/-}$) mouse platelets, which mimic the bleeding disorder Glanzmann thrombasthenia in patients, formed filopodia and did not spread on Fn but did spread largely normal on Ln (fig. S11A). In contrast to our αIIbβ3 inhibitor studies, the formation of Fn fibrils beneath the cells on Ln was not completely suppressed but partially still intact (fig. S11B). Together, α5β1 is thus dispensable for Fn assembly by platelets and cannot rescue fibrillogenesis upon blockage of αIIbβ3 integrins but does so in αIIb-deficient platelets.

Partial inhibition of αIIbβ3 by low dose of RUC-2 (3 μM) or 10E5 (3 μg ml^{-1}) still allowed normal platelet spreading on Fn coatings (fig. S10A) yet had a major impact on Fn fibrils that were now pulled along the basal and not along the apical membrane (Fig. 4, F to I), similar to fibrils on Ln coatings. A concentration of 3 μM RUC-2 corresponds to an inhibition of αIIbβ3 integrins by 99.2% confidence interval: (84.8%, 99.99%) as determined by binding of fluorescently

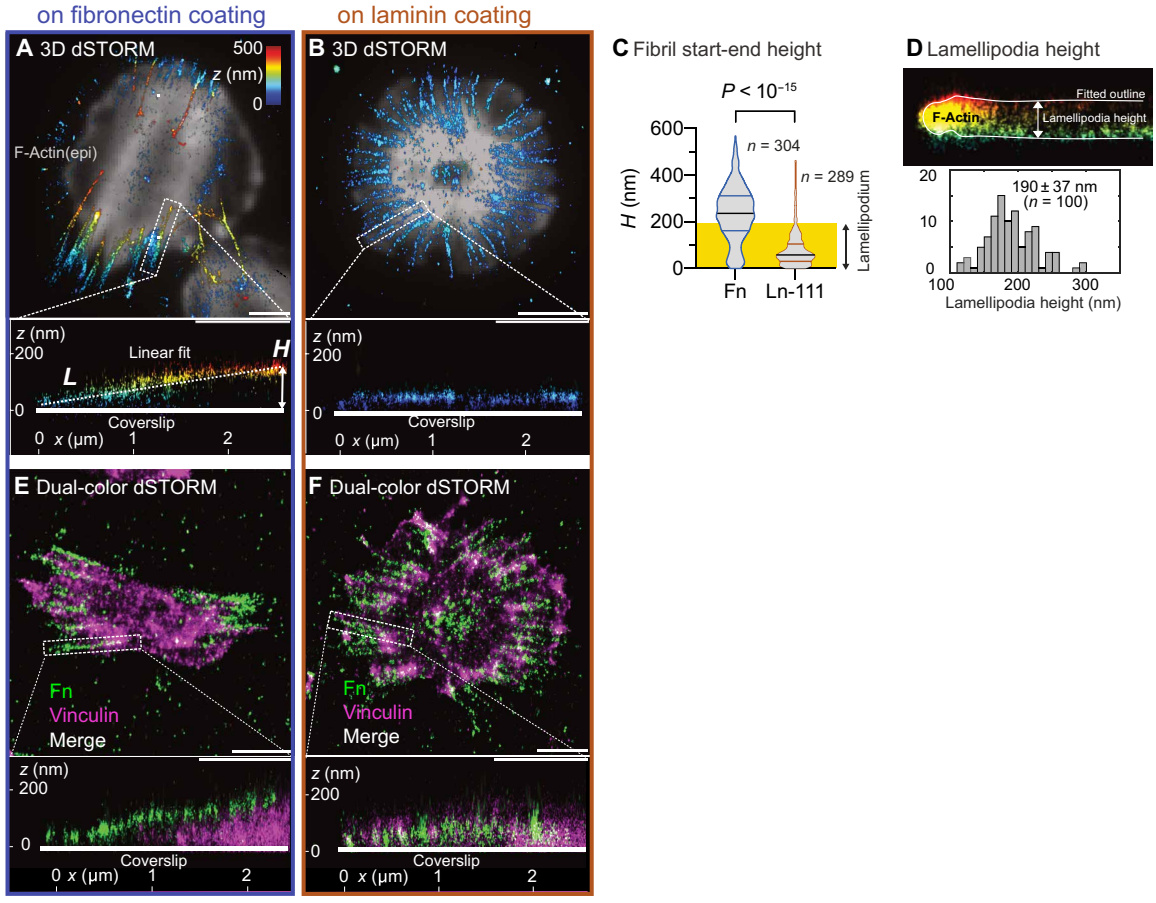

Fig. 3. Analysis of the dimensionality of Fn fibrils assembled by human platelets seeded on Fn and Ln coatings. (**A**) 3D STORM of Fn fibrils assembled by a representative platelet spread on Fn-coated glass. The *z* position of pFn647 is color-coded from blue (basal) to red (apical). All STORM images are overlaid onto an epifluorescence (epi) image of F-actin (gray). Bottom: Side view of a single Fn fibril [boxed region in (A)] and linear fit (dashed line) yielding the length *L* and the height *H* of the fibril. (**B**) Fn fibril assembly by a representative platelet spread on a Ln-111–coated coverslip. Note the nonstraight appearance of Fn fibrils on Ln-111. Bottom: Side view of a single Fn fibril [boxed region in (B)]. (**C**) Comparison of Fn fibril height on Fn coatings (blue) and Ln-111 coatings (brown). The yellow background denotes the lamellipodia height. Data were pooled from nine donors (24 to 35 years). Only fibrils longer than 1 μm were included in the analysis; for donor-to-donor variation on Fn and Ln-111 coatings, see fig. S2. Data were compared using an unpaired two-tailed Mann-Whitney test. (**D**) Analysis of lamellipodia height of spread platelets on Fn (cf. fig. S8). One hundred regions in 13 spread platelets were analyzed. (**E**) Dual-color 3D STORM of pFn647 (green) and vinculin (magenta) in a representative platelet spread on Fn. Bottom: Side view of a single Fn fibril [boxed region in (E)]. (**F**) Dual-color 3D STORM of pFn647 (green) and vinculin (magenta) in a representative platelet spread on Ln. Bottom: Side view of a single Fn fibril [boxed region in (F)]. Scale bars, 2 μm (A, B, E, and F).

labeled Fg to crosslinked collagen-related peptide (CRP-XL)–activated platelets (fig. S12). Since this finding suggested that altered signaling downstream of integrin β3 could regulate 3D versus 2D fibril assembly, we measured the phosphorylation of integrin β3 tails and of integrin-linked kinase (ILK) by Western blot. Integrin β3 phospho-Tyr^{773} was detected in platelets on Ln and Fn but was 1.8-fold more pronounced on Fn (Fig. 4J). While the latter was expected because αIIbβ3 integrins mediate platelet adhesion and spreading on Fn, the prior band is evidence of a cross-activation of β3 on Ln. We further found that ILK activation was much stronger in platelets on Fn compared to Ln (Fig. 4K). Since ILK plays a crucial role for the maturation of fibrillar adhesions in fibroblasts (*26*, *27*), its strong activation in platelets on Fn could point toward a potential role for orchestrating the dimensionality of Fn fibrils.

Emerging fibrillar adhesions in fibroblasts contain talin, which binds to the NPxY motif of β1 integrins as well as to actin, while, over time, talin is being replaced to variable extents by tensin controlled by phosphorylation of the NPxY motif (*28*). In contrast to fibroblasts (fig. S13), and although we did observe specific tensin-1 immunostaining, tensin-1 in platelets did not localize to adhesion sites but rather to centrally located granules (fig. S14).

Talin is more strained in apical than in basal fibrillar-like adhesions on Fn versus Ln coatings

To gain more detailed morphological insights into fibrillar-like adhesions in platelets, we used dual-color STORM to characterize their molecular build-up. When Fn-bound integrins are coupled via talin to actin fibers, which are pulled via myosin II, talin gets stretched and partially unfolds, opening up binding sites for vinculin molecules that re-enforce these molecular linkages during adhesion maturation (*29*). Talin unfolding is accompanied by an increasing spatial offset between integrins and vinculin (*30*). In platelets spread on Fn, vinculin was strongly localized to peripheral adhesion sites and formed string-like patterns that were coaligned with F-actin bundles

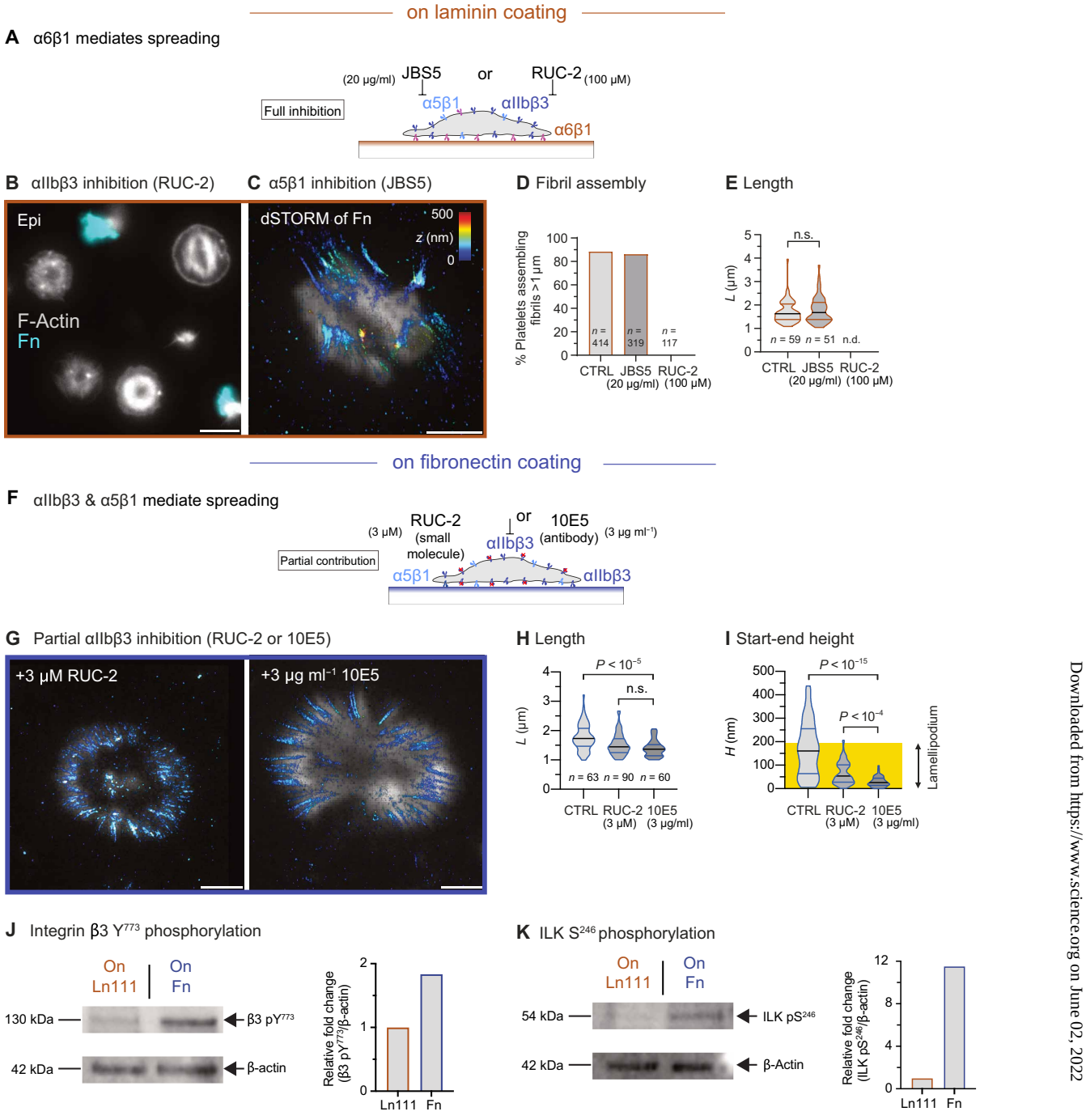

Fig. 4. Contributions of α5β1 and αIIbβ3 integrins to Fn fibrillogenesis by platelets. (**A**) Saturating concentrations of the blocking antibody JBS5 (20 μg ml^{-1}) against α5β1 or of the nonpriming inhibitor RUC-2 (100 μM) against αIIbβ3 were supplemented during platelet seeding on Ln-111–coated glass coverslips. Platelets spread on Ln using α6β1 integrins independent of the blocked integrins. (**B**) Epifluorescence image of F-actin (gray) and pFn647 (cyan) of platelets inhibited with RUC-2 (100 μM). (**C**) 3D STORM of Fn fibrils (*z* color code) overlaid onto an epifluorescence F-actin image (gray) of a platelet inhibited with JBS5 (20 μg ml^{-1}). (**D**) Fraction of platelets that produced micrometer-long fibrils in the absence or presence of JBS5 and RUC-2, respectively. (**E**) Fn fibril length for platelets treated with JBS5 or RUC-2. Data were obtained from three donors (28 and 34 years). No fibrils were detected for RUC-2 (n.d., not detectable). (**F**) Subsaturating concentrations of the nonpriming αIIbβ3 inhibitor RUC-2 (3 μM) or of the blocking antibody 10E5 (3 μg ml^{-1}) against αIIbβ3 were supplemented during platelet seeding on Fn-coated glass coverslips. (**G**) 3D STORM of Fn fibrils assembled in the presence of 3 μM RUC-2 (left) or 10E5 (3 μg ml^{-1}) (right). (**H** and **I**) Fibril dimensions for partial αIIbβ3 inhibition. Data were pooled from two donors (28 to 35 years) and compared with an unpaired two-tailed Mann-Whitney test. (**J** and **K**) Cell lysates of platelets seeded on Ln-111– or Fn-coated coverslips were separated by SDS–polyacrylamide gel electrophoresis and stained for (J) integrin β3 pY^{773} or (K) integrin-linked kinase (ILK) pS^{246}. The level of protein phosphorylation was quantified and normalized by β-actin. Scale bars, 5 μm (B) and 2 μm (C and G).

(*19*). Fn fibrils overlapped with these elongated vinculin patterns and were tightly registered (Figs. 3E and 5A), similar to fibrillar adhesions in fibroblasts (*31*). Analysis of the localization density along linear vinculin-Fn patterns (fig. S15A), where vinculin decorates stretched talin, revealed a mean spatial offset of 381 ± 195 nm between the terminal ends of Fn fibrils and vinculin patches (n = 60; Fig. 5, D and E). A similar mean offset of 375 ± 278 nm is seen for fibroblasts on Fn coatings (fig. S15, C and D). On Ln coatings, the offset between vinculin and Fn was only 157 ± 90 nm (n = 64; Fig. 5, C and E, and fig. S15B) and thus significantly smaller. The offset between Fn and vinculin decreased even more after partial inhibition of αIIbβ3 integrins (38 ± 37 nm, n = 37; Fig. 5, B and E). The observed offset range is consistent with measured force-induced talin rod extensions of 60…350 nm (*32*) and the measured shallow orientation ~15° of talin within adhesions (*22*). This suggests that the mechanical strain of the integrin-talin-vinculin-actin connections that are part of force-bearing apical fibrillar adhesion sites in platelets on Fn is significantly larger than in basal fibrillar-like adhesions on Ln coatings. (Immunohistochemical stains in platelets for talin and the integrin αIIbβ3 as well as 3D STORM images of fibroblasts stained for vinculin versus α5 and for Fn versus α5 are provided in fig. S16.)

Platelet contractility is significantly higher on Fn than on Ln coatings

We next asked whether the different strain in fibrillar-like adhesions on different protein coatings is related to different levels of platelet contractility. We thus measured traction forces generated by single platelets across cell-substrate adhesions using micropost arrays that were coated with Fn or Ln by microcontact printing and then passivated to restrict adhesion of platelets to the functionalized post tops (Fig. 6A). Platelets spread similarly on either coating and bent posts toward the center of the cell (Fig. 6, B and C). A quantification of post deflections yielded higher tractions on Fn compared to Ln, with 2.7 ± 1.6 nN versus 2.0 ± 1.3 nN mean force per post or 21.6 ± 14.9 nN versus 15.3 ± 11.0 nN total force per cell, respectively (Fig. 5, D and E). The total force per cell, as calculated from the nonvectorial sum of force magnitudes over many posts on Fn, was comparable to individual platelets pulling at two anchoring points, i.e., at a suspended AFM tip and a Fg-coated substrate (*33*) or two nearby Fg dots on a compliant polyacrylamide hydrogel (*3*). Partial αIIbβ3 inhibition by RUC-2 (3 μM) significantly reduced tractions on Fn to below the levels on Ln (Fig. 5, D and E). Since Fn and Ln coatings on microposts were prepared by the same technique with

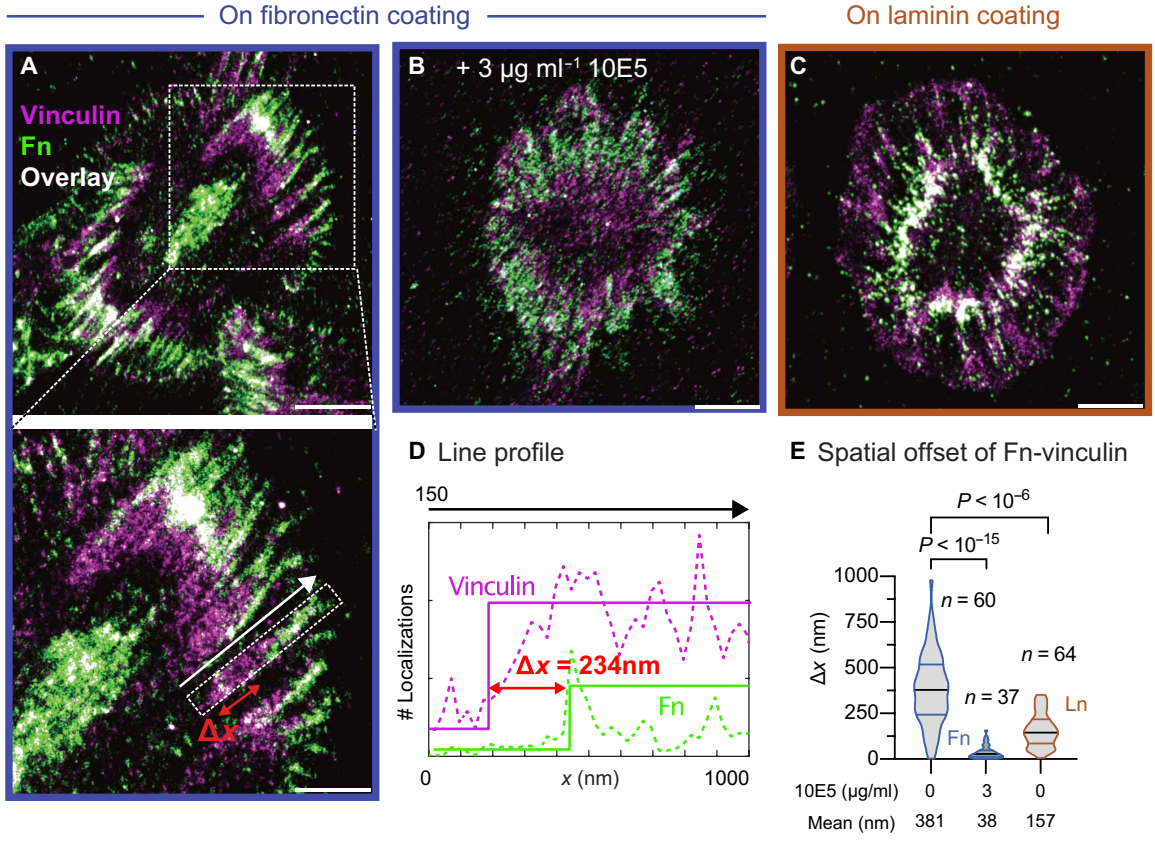

Fig. 5. Nanoscopic analysis of fibrillar-like adhesion molecular morphology. (**A**) Dual-color STORM image of pFn647 (green) and vinculin (magenta) in a representative platelet spread on Fn-coated glass. Bottom: Magnified view of the boxed region in (A) along a Fn fibril. Red arrow (Δx) denotes the spatial offset of the vinculin stain with respect to the Fn fibril. (**B**) Representative platelet seeded in the presence of subsaturating concentrations of the αIIbβ3 blocking antibody 10E5 (3 μg ml^{-1}) on Fn-coated glass. Same representation as in (A). (**C**) pFn647 (green) and vinculin (magenta) in a representative platelet spread on Ln-111–coated glass. Same representation as in (A). (**D**) Exemplary line profiles (dashed) of the density of fluorophore localizations along the line in (A) for the vinculin stain (magenta) and the pFn stain (green). Each profile was approximated by a step function to obtain the spatial offset Δx between stains. (**E**) Spatial offset between Fn fibrils and vinculin for platelets on Fn, on Ln-111, or on Fn with partial inhibition of αIIbβ3. Platelets were obtained from three donors (28 to 34 years). Data were compared using Kruskall-Wallis rank test with post hoc Dunn's test. Scale bars, 2 μm (A to C) and 1 μm (A, magnified view).

no detectable differences in the coating efficiency (fig. S17), this important finding suggests that the ECM proteins to which platelets adhere as well as the number of binding-competent adhesion receptors directly regulate platelet traction forces.

Since cellular traction forces are known to direct Fn fibrillogenesis (*20*), although it is unclear whether this relationship is causative or correlative, we used blebbistatin (BBT) which inhibits human myosin IIa with an IC_{50} (median inhibitory concentration) of 5.1 μM. Blocking contractility with a high dose of BBT (20 μM) led to lessened F-actin bundling and nearly completely abolished the formation of Fn fibrils (fig. S18, D to I) in agreement with reports in fibroblasts (*20*, *34*). BBT concentrations between 0.3 and 10 μM dose-dependently reduced the fraction of fibril-forming platelets from 80 to 20% but hardly affected fibril diameter and length nor their apical anchorage (fig. S18, E to H). Three and 10 μM BBT significantly reduced mean platelet traction forces but still showed a minor fraction of platelets with elevated contractility (fig. S18I). *Myh9*-related disease in patients is associated with compromised hemostasis, and a common disease variant is carrying the mutation D1424N. Platelets from a mouse model of this disease phenotype (*35*), which is associated with by ~40% reduced traction forces of single platelets *(36)*, assembled Fn fibrils with apparently the same efficiency than platelets from wild-type mice (fig. S11C). In summary, while partial myosin IIa inhibition directly reduced single-platelet traction forces, only higher inhibitor concentrations affected Fn fibrillogenesis in an apparent all-or-none fashion, similar to the inhibition of Rac-1 and Cdc-42 (cf. Fig. 2J and fig. S5) but in contrast to the gradual (3D to 2D) effect of αIIbβ3 adhesion receptor partial inhibition (cf. Fig. 4, F to I).

Fn fibril networks of different dimensionality are a ubiquitous feature of platelet-assembled ECM in contact with clot versus basement membrane proteins

We lastly asked whether our findings regarding Fn assembly could be generalized to specific thrombus sites. In the developing thrombus, "procoagulant" phosphatidylserine (PS) exposure on platelets stimulates the activation of clotting factors that catalyze Fg to Fb conversion and cross-linking. We thus selected Fb as the major clot component since spreading on Fb, but not Fg, supports Fn matrix assembly by platelets (*16*). Platelets on Fb coatings showed the typical

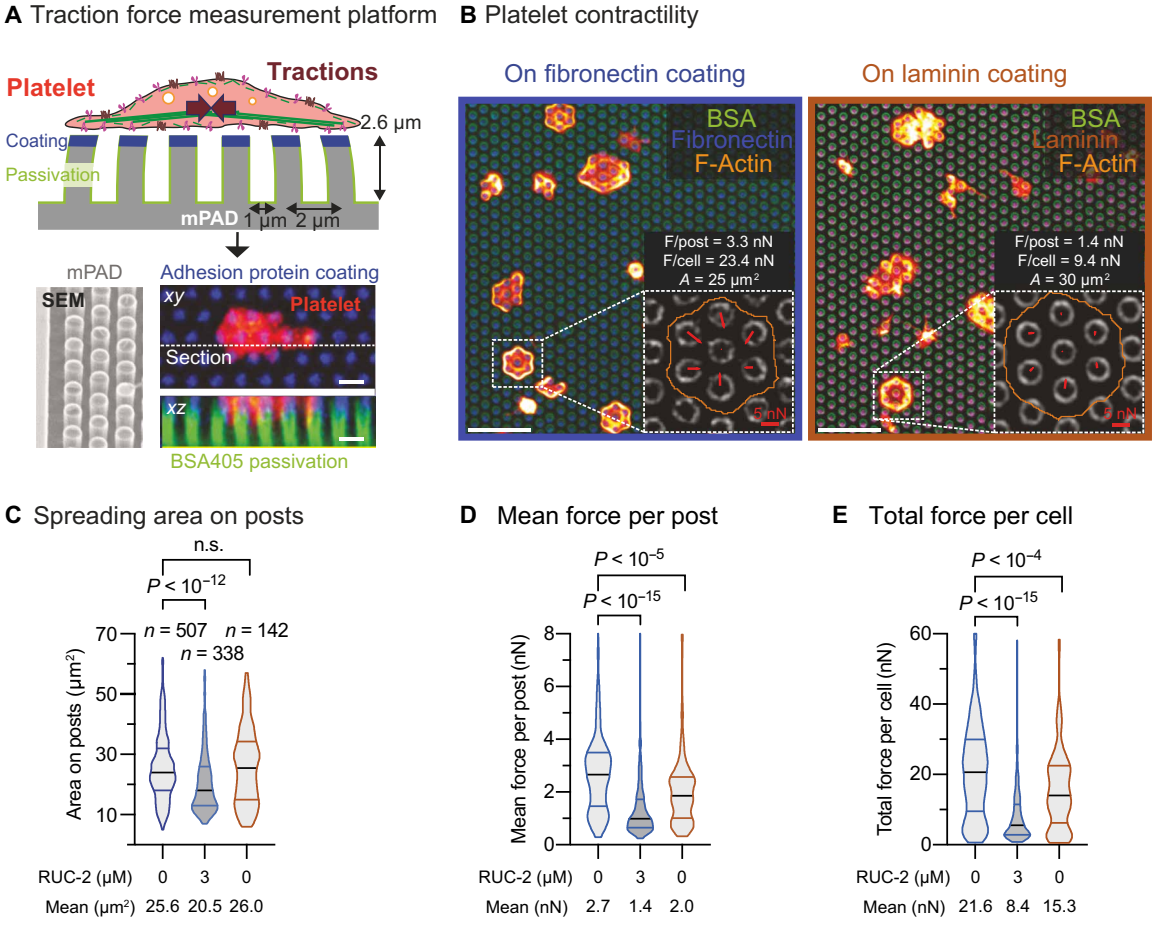

Fig. 6. Cell-substrate tractions of platelets on Fn and Ln. (**A**) Traction forces of single platelets are measured with an optimized micropost array. The tops of the posts are stamped with the respective proteins (blue) and the side walls are passivated (green). Post deflections are determined from the centroids of posts in confocal slices using fluorescently labeled bovine serum albumin (BSA) (green). (**B**) Platelets are seeded for 1 hour on microposts arrays coated with Fn (left) or Ln-111 (right) and then fixed and stained for F-actin (red hot color map). Insets: Force distribution (red arrows) and measured values of a representative platelet (white boxed region). Force scale bars, 5 nN. (**C** to **E**) Comparisons between Fn and Ln-111 in terms of (C) spreading area on posts, (D) the mean force per post, and (E) total force per platelet. The total force per cell is the sum of the magnitude of forces acting on individual posts beneath a single cell, not their vectorial sum. Data were pooled from four donors (33 to 43 years). Data were compared using an unpaired two-tailed Mann-Whitney test. Scale bars, 10 μm (B) and 2 μm (A).

bipolar phenotype (*19*) and formed Fn fibrils mainly localized in the periphery at two opposing ends of the cell (Fig. 7A). As on Fn coatings, Fn fibrils on Fb were mainly pulled along the apical membrane (Fig. 7C), and only a moderate increase in fibril length and thickness were noted (fig. S19). Besides Ln, collagen type IV (Col4) is the most abundant component of the vascular basement membrane. Fn fibrils on Col4 coatings (Fig. 7B) recapitulated the architecture on Ln with respect to their anchorage beneath the cell (Fig. 7C), length, and thickness (fig. S19). Platelet traction forces on Col4 were of similar magnitude as on Ln, while forces on Fg were significantly higher (Fig. 7D).

To address the situation where many platelets adhere to an endothelial lesion during thrombus formation, we seeded washed platelets at higher density on Ln-coated glass and characterized the formed Fn matrix beneath, around, and between surface-bound aggregates by 3D dSTORM over an extended *z* range (Fig. 7E and fig. S20). Like in single platelets, extensive Fn fibrils were formed beneath the cells on Ln (asterisks). In addition, many short Fn fibrils were observed higher up from the coverslip between platelet-platelet contacts within aggregates (arrows). Longer 3D fibrils (filled arrowheads) up to 10 μm length were formed at the edges of aggregates, and also between aggregates, preferentially along filopodial bridges (hollow arrowheads).

To investigate whether platelets can form Fn matrix in the context of a blood clot, we coagulated whole blood in the presence of fluorescently labeled Fn and Fg by addition of $CaCl_2$ and imaged Fn in relation to the Fb mesh by lattice light sheet microscopy (Fig. 7F). As expected, soluble Fn bound to and decorated Fb fibrils evenly across the field of view (overview). However, distinct and extensive Fn deposits that were separate from Fb fibers were observed in hotspots around radially bundled Fb fibers (insets). The hotspots are connected by straight Fb fibers which indicate that they represent contractile platelet aggregates (*37*).

In summary, platelets formed a planar Fn matrix on basement membrane proteins and a 3D matrix in contact with clot proteins or within clot protein-mediated platelet aggregates, accompanied by low and high traction forces, respectively.

DISCUSSION

How local biochemical and mechanical cues are sensed by platelets and direct their response toward a spatiotemporal well-orchestrated repair of injured vessel walls still remains elusive. As mediated by αIIbβ3 integrins, we found here that platelets robustly assemble Fn fibrils in contact with various ECM proteins in two spatially distinct architectures when adhering to thrombus versus basement membrane proteins (Figs. 1 to 3 and 7), respectively, which correlate with differentially up-regulated platelet contractility (Figs. 6 and 7). This de novo Fn fibrillogenesis by platelets is in line with previous observations made at lower optical resolution on platelets alone (*13*, *16*) or in blood clots (*7*). The Fn fibrils show linear coalignment with F-actin (Fig. 2I) and a pronounced stretch-induced offset of the adaptor protein vinculin from the integrin adhesions (Fig. 5). The qualitatively similar Fn fibril deposition characteristics of platelets compared to fibroblasts in terms of apical versus basal Fn fibril anchorage on different ECM coatings (Figs. 3 and 7) and the contractility dependence of Fn deposition (Fig. 6) point toward morphological and functional similarities in their formation mechanisms. Fibrillar adhesions in fibroblasts are elongated adhesion structures (micrometer wide and several micrometers long), associated with contractile actin filaments and with Fn fibers, on either the apical or basal side, and located more centrally (*10*, *31*, *38*), in contrast to focal adhesions which only form on the basal side and more peripherally. Because of the small size of platelets, the displacement of fibrillar-like adhesions from the original site where fibrillogenesis was initiated remains small, and the length of the corresponding fibrils is limited to ~1 to 2 μm. Certain cell-substrate adhesion signaling and mechanotransduction processes important for Fn fibrillogenesis, which are well established for fibroblasts (*39*), might thus be shared by platelets, although platelets use αIIbβ3 integrins rather than α5β1 integrins to drive Fn fibrillogenesis (Fig. 4). Beyond thrombus formation and contraction, these roles of αIIbβ3 integrins and of platelet contractility in the assembly of the first provisional Fn matrix have so far not been recognized.

Our experiments not only visualized that Fn nanofibrils exist but also revealed different Fn fibril architectures pulled by platelets, as first visualized here as it requires superresolution microscopy (Fig. 2). When making their first contact with Fn, platelets pulled the earliest Fn fibrils along their filopodia, while tiny fibrils perpendicular to the cell edge were formed during subsequent lamellipodial spreading. As a common theme between platelets on different adhesion proteins, the most pronounced Fn fibrils were pulled only after platelets had rearranged and formed a stable F-actin cytoskeletal arrangement (Fig. 2 and figs. S3 and S4), thus after spreading was complete (*19*). Fn fibrils were typically pulled along stress fibers from opposite ends at the apical membrane on Fn and radially inward toward a contractile actin ring along the basal membrane on Ln (Figs. 1 to 3). Fn clumps located more centrally shared the same *z* localization as these major Fn fibrils, pointing toward a common origin. We speculate that these Fn clumps might arise from Fn fibril rupture at the substrate contact point. Once ruptured, the images give hints that the fibers recoil toward the adhesion site that anchors them at the platelet, before this adhesion site disassembles as a consequence of the released force. The fraction of platelets assembling major Fn fibrils could be reduced by direct inhibition of either myosin IIa activity (fig. S18) or Rac-1 or Cdc42 (Fig. 2J and fig. S5) acting upstream of actin dynamics and myosin contractility. Since Rac-1 is known to be essential for migration, the blocking experiments rule out that the main Fn fibrils are formed during retraction.

Integrin αIIbβ3 fulfills all requirements to drive Fn fibrillogenesis in platelets as it has a synergy site like α5β1 important for reinforcing cell adhesion (*17*, *23*). Although α5β1 integrins compete with αIIbβ3 for their common ligand Fn, they make minor contributions to fibril assembly in platelets and cannot rescue fibril formation upon αIIbβ3 inhibition (Fig. 4) but do so in αIIb-deficient platelets (fig. S11B). Fibrillar adhesion formation and Fn assembly as known from fibroblasts require the recruitment of talin and kindlin to form the ternary IPP (ILK, PINCH1, and α-parvin) complex to the cytosolic tail of β-integrins (*26*), which lastly recruits tensin (*40*). This mechanism is conserved across fibroblasts (*26*, *27*), endothelial cells (*41*), and epithelial cells (*42*). In all these cell types, α5β1 integrins drive Fn fibrillogenesis (*9*), yet αvβ3 can partially compensate in the absence of α5β1 (*43*). While talin links integrins to F-actin, kindlins promote integrin clustering and thus modulate the avidity at the adhesion site (*44*). Platelets, unlike fibroblasts, do not have kindlin-2, but their unique platelet kindlin-3 equally promotes integrin β1 and β3 clustering (*45*). In activated platelets, ILK interacts with either β1 or β3 integrins (*46*, *47*), induces β3 phosphorylation (*48*), and affects

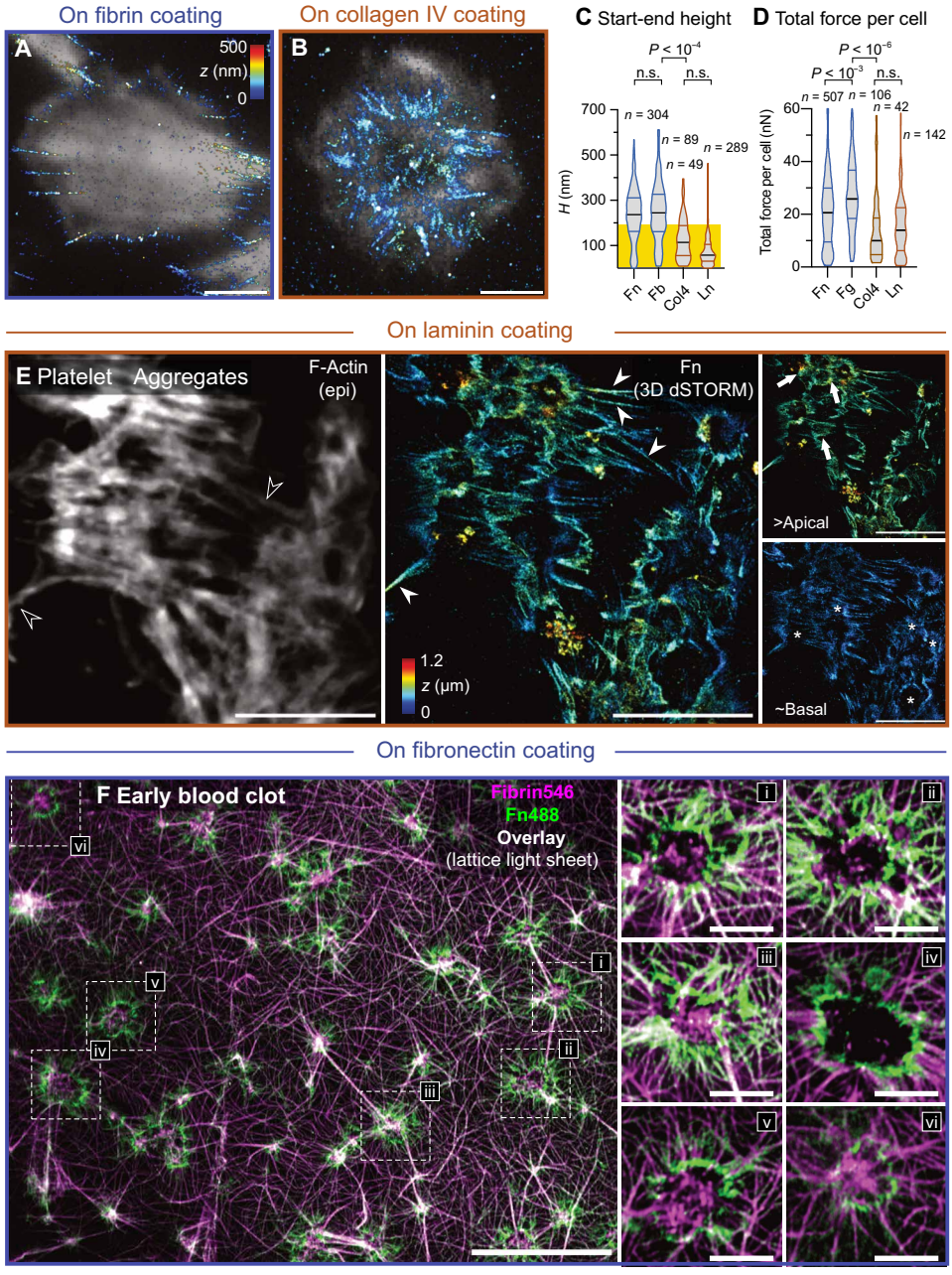

Fig. 7. Fn fibrillogenesis by platelets in the context of basement membrane proteins or clot proteins. (**A**) 3D STORM image of pFn647 of a single platelet seeded on Fb (binds αIIbβ3) overlaid onto an epifluorescence (epi) image of F-actin (gray). (**B**) 3D STORM image of pFn647 of a single platelet seeded on Col4 (binds α2β1) overlaid onto an epifluorescence (epi) image of F-actin (gray). (**C**) Fibril start-to-end height between Fn, Fb, Col4, and Ln-111. Data were pooled from four donors (33 to 43 years) and were compared with a nonparametric Kruskall-Wallis rank test with post hoc Dunn's test to make multiple comparisons. (**D**) Platelet traction forces on Fn, Fg, Col4, and Ln-111–coated micropost arrays. (**E**) Epifluorescence image of F-actin (left) and 3D STORM image of pFn647 (middle) of platelet aggregates formed on Ln. Note that the color code corresponds to an extended z-range of 1.2 μm. Right: *z* slices showing the upper 0.8 μm (top) or lower 0.4 μm (bottom) of the STORM data (same color code). (**F**) Lattice light sheet micrograph of Fn (green) and Fb (magenta) in a clot formed from whole blood on a Fn-coated surface. Left: Average intensity projection of the stack. Right: Selected slices of the boxed regions in (E). Scale bars, 50 μm (F), 10 μm (E and F, insets), and 2 μm (A and B).

late adhesion signaling (*47*). The IPP complex is also recruited to overexpressed αIIbβ3 integrins in Chinese hamster ovary cells (*49*), which can assemble Fn matrix (*50*). Although tensin is neither essential for fibrillar adhesion formation nor for Fn assembly (*27*), it rather associates with fibrillar adhesions after being recruited by IPP (*26*). While the reason why tensin did not localize to fibrillar-like adhesions in platelets (fig. S14) remains unclear, we propose that this unexpected finding, as well as the apparent discrepancy between αIIbβ3 inhibition experiments and αIIb knockouts, can be explained by competition between αIIbβ3 and α5β1 integrins for their common binding partners, talin and kindlin. Talin binding affinities for β-integrin tails are relatively weak, with a relatively

higher affinity for β3 (273 μM) compared to β1A (491 μM) (*51*). Weak binding interactions critically depend on the relative abundance of binding partners. In platelets, β3 is about 6 times more abundant than β1, and αIIb is about 40 to 60 times higher expressed than α5 or αV (*24*, *25*). One possibility is that αIIbβ3 integrins outcompete α5β1 in their quest to bind talin or kindlin, resulting in the trans-dominant inhibition of the less abundant integrin (*52*), analogous to the previously reported trans-dominant inhibition of α2β1 by αIIbβ3 in platelets (*53*). Together, we propose that a trans-dominant inhibition of β1 by β3 integrin tails might be maintained in the presence of αIIbβ3 inhibitors, thus preventing α5β1 from rescuing Fn fibrillogenesis, while α5β1 can normally form Fn fibrils in the case of Glanzmann thrombasthenia, where β3 integrin expression levels are substantially reduced. Talin binds to the membrane proximal NPxY motif of β-integrins in emerging fibrillar adhesions and is over time replaced to variable extents by tensin (*38*) controlled by phosphorylation of the NPxY motif (*28*). Whether the >100-fold excess of talin-1, together with the >60-fold excess of αIIbβ3, over tensin-1 in human platelets (*25*), or different binding modes and affinities for β3 versus β1A cytoplasmic tails of their binding partners tensin (*54*), talin (*51*), or other adaptor proteins (some of which have unique roles in platelets, such as kindlin-3 or hic-5) might hinder an efficient association of tensin with αIIbβ3 integrins during the here studied early phases of Fn fibrillogenesis in platelets warrants further investigations.

In platelets, adhesion signaling of either α6β1 on Ln, α2β1 on Col4, or αIIbβ3 on Fn or Fb stimulates αIIbβ3 integrins to assemble Fn fibrils (Figs. 1 to 3 and 7), analogous to the preactivation of α5β1-driven fibrillogenesis by αvβ3 in fibroblasts on Fn (*31*, *55*) and α3β1 or α2β1 on Matrigel (*10*), and in accordance with previous observations (*13*–*16*). As a common theme between platelets and other cells, β1-mediated cell-substrate interactions resulted in the basal deposition of planar Fn fibrils, while β3-mediated cell adhesion resulted in apical 3D fibrils. Adhesion signaling through αIIbβ3 led to increased phosphorylation of β3 integrins and ILK (Fig. 4, J and K) and was essential to develop high platelet contractility, maximal stress fibers (*19*), a 3D apical anchorage of Fn fibrils (Fig. 3), and an elevated mechanomolecular strain within fibrillar-like adhesions (Fig. 5). Partial inhibition of αIIbβ3 integrins on Fn resulted in 2D Fn fibrillogenesis (Fig. 4) and in significantly reduced traction forces (Fig. 6). A previous study showed that higher αIIbβ3 ligand densities, and thus more engaged αIIbβ3 integrins, shifted signaling downstream of αIIbβ3 from focal adhesion kinase and Syk to class I phosphoinositide 3-kinase (PI3K) (*56*). PI3K signals through Akt to activate RhoA, which increases myosin light chain phosphorylation (pMLC) through Rho-associated protein kinase (ROCK), thereby enhancing binding of myosin II to F-actin and up-regulating cellular contractility (*40*). PI3K also activates ILK in platelets (*46*, *48*). Notably, deficiencies of either component of these signaling pathways lead to impaired thrombus stability (*40*). Both signaling pathways are also important for 3D Fn fibrillogenesis in fibroblasts (*26*, *34*), while the basal formation of Fn fibrils by endothelial cells proceeded even after RhoA silencing in the absence of obvious actin stress fibers but at apparently unchanged pMLC levels (*11*). We thus propose that ECM proteins from the vessel wall and the thrombus have instructive power directing platelets to adopt distinct phenotypes of medium and high contractility, which coordinate 2D and 3D fibrillogenesis, respectively, as mediated through ILK activation downstream of integrin outside-in adhesion signaling that depends on both, integrin isoform and numbers (Fig. 8 and Movie S1).

Extrapolating from our findings, we propose here that the dynamic tuning of platelet mechanobiology by rapidly changing environmental factors is exploited during thrombus formation and remodeling, which itself is a highly dynamic process, to ensure a sufficient and continuous mechanical stability from plaque formation through wound contraction. The heterogeneous ECM microenvironment at wound sites might direct location-specific responses, which, upon integration, steer the early phases of a spatially well-organized tissue repair process. Although many of these previously unidentified concepts need to be verified in vivo, we, in the following, would like to shortly discuss potential implications of our findings.

The Fb- and Fn-rich extraluminal thrombus portion in penetrating injuries (*8*, *57*) could locally enhance compaction by maximizing platelet contraction. Contractile platelets were shown to expel non-contractile, nonadhesive procoagulant platelets to the thrombus surface (*58*). Graded platelet contractility could thus orchestrate the local packing density of platelets within the developing thrombus, resulting in the core shell architecture (*59*). The progressive development of a 3D network of Fn fibrils in the thrombus core (see Fig. 7F) might guide infiltrating cells or allow migrating platelets (*5*) to reposition themselves within a lesion. This interpretation is in agreement with our previous observations of Fn fibrillogenesis and fibroblast invasion made on 2- and 24-hour-old blood clots that had formed on titanium surfaces (*7*).

Platelets of medium contractility could mediate the thrombus anchorage at the vascular basement membrane upon superficial injury. Planar Fn fibril networks at the basement membrane debris could help to restore the tissue barrier by providing a template for the reassembly of collagens or basement membrane repair, or by guiding cell migration as during vascular morphogenesis (*6*, *10*). This interpretation is in agreement with data showing that the planar Fn matrix that endothelial cells self-deposit at their basal side promotes endothelial monolayer integrity and directs endothelial plasticity (*12*). Fn matrix deposited on basement membrane could, in the case of platelet detachment, moreover contribute to local concentration differences of αIIbβ3 integrin ligands that have been shown to steer platelet haptotaxis in the context of inflammatory bleeding (*5*).

While further studies are required to determine how platelets integrate the sensing of ECM identity, substrate stiffness (*60*, *61*), and additional chemical stimuli like gradients of platelet agonists or PS exposure to up- (*13*) or down-regulate (*61*) platelet contractility, our results strengthen the emerging central tenet in the field that platelet contractility is not only a tightly regulated function but is also tuned by outside-in signaling. Our finding that microenvironmental sensing of protein identity regulates platelet contractility and goes hand in hand with the spatial architecture of the first provisional Fn matrix establishes a so far unrecognized link between the hemostatic function of platelets and their potential initial contributions to early wound repair and healing processes. These findings are prone to stimulate further verifications within relevant pathophysiological contexts.

METHODS

Reagents

The following reagents were purchased from Sigma-Aldrich, if not mentioned otherwise. Acid citrate dextrose (ACD) tubes (Sol. B,

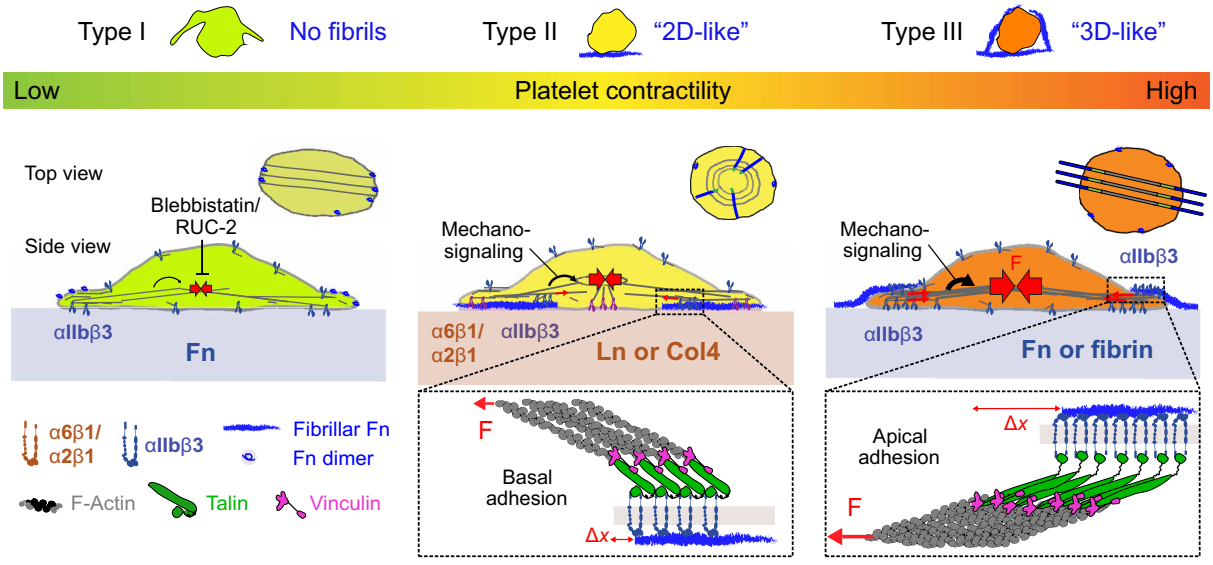

Fig. 8. Integrin mechanosensing of ECM proteins triggers dimensionality of the first deposited ECM network. Schematic summary of results. Platelets spread on Fn and Fb (right) generate high traction forces (red arrows and dark red-yellow) and Fn fibrils are aligned to polarized actin bundles (top view). Mechanosignaling (black arrow) through αIIbβ3 (blue) instructs Fn fibril anchorage along the apical membrane of platelets and the mechanomolecular strain induces a spatial offset between vinculin (green) and Fn (see inset). On Ln or Col4 (middle), platelets contract less strong (yellow) and form radial oriented Fn fibrils (top view) pulled beneath their basal side with a small spatial offset between vinculin and Fn (side view, inset). Dose-dependent inhibition of myosin IIa and the αIIbβ3 (left) further reduces platelet contractility (green) and prevents Fn fibril formation.

Vacutainer, BD, Switzerland); coverslips (18 mm in diameter; thickness, 1.5; Hecht-Assistent, Germany); human Fg (F3879); human Fn [purified from plasma as described previously (*62*)]; human Col4 (C8374); murine Ln (Ln-111; L2020); human Ln (Ln-521, Biolaminin521 LN, BioLamina, Sweden); bovine serum albumin (BSA; 05470); adenosine 5′-diphosphate sodium salt (ADP; A2754); thrombin from human plasma (T6884); RUC-2 and 10E5 (gift from B.S. Coller, New York University); BBT (B0560); Nsc23766 trihydrochloride (SML0952); ML 141 (SML0407); mouse anti-integrin α5β1 (MAB1969); mouse anti-vinculin (V9131); rabbit anti-tensin 1(SAB4200283); mouse anti–β-actin (ab8226, Abcam, UK); rabbit anti–phospho-ILK (Ser^{246}) (AB1076); rabbit anti-integrin beta 3 (phospho Y773) (ab38460, Abcam, UK); unconjugated donkey anti-mouse or anti-rabbit immunoglobulin G (IgG) (Jackson Immunoresearch, USA); horseradish peroxidase (HRP)–conjugated donkey anti-rabbit or anti-mouse IgG (Jackson Immunoresearch, USA); Alexa Fluor 647 *N*-hydroxysuccinimide (NHS) ester (A20006, Thermo Fisher Scientific, USA); CF680 NHS ester (92139, Biotium, USA); Alexa Fluor 546 NHS ester (A20002, Thermo Fisher Scientific, USA); DyLight 405 NHS ester (A46400, Thermo Fisher Scientific, USA); goat anti-mouse CF680 (SAB4600361); Alexa Fluor 488 Phalloidin (A12379, Thermo Fisher Scientific, USA); Alexa Fluor 647 Phalloidin (A22287, Thermo Fisher Scientific, USA); human Factor XIII (Fibrogammin 1250, CSL Behring); phosphatase inhibitor (P5726); protease inhibitor (11836170001); bicinchoninic acid (BCA) protein assay kit (23225, Thermo Fisher Scientific, USA); Western Blotting Substrate (32209, Thermo Fisher Scientific, USA); Mini SFX gels (4568093, Bio-Rad, USA); Float-A-Lyzer G2 molecular weight cutoff 20-kDa dialysis columns (Z726834-12EA); TI Prime (MicroChemicals, Germany); photoresist AZ 1505 (MicroChemicals, Germany); developer AZ 726 MIF (MicroChemicals, Germany); Sylgard 184 Silicone Elastomer (Dow Corning, USA); hard polydimethylsiloxane (PDMS) (PP2-RG07, Gelest, USA); and Trichloro(1*H*,1*H*,2*H*,2*H*-perfluorooctyl)silane (448931) and Pluronic F-127 (P2443).

Labeling of plasma Fn and BSA with fluorescent dyes

Purified Fn [in 1 M arginine in phosphate-buffered saline (PBS)] was stored at −80°C before use. The random labeling of surface accessible lysine residues of Fn was achieved by amid bond formation with fluorescent probes as described previously (*62*). Briefly, Fn was transferred into an amine labeling buffer [0.1 M $NaHCO_3$ in PBS (pH 8.5)] and incubated with 20-fold molar excess of Alexa Fluor 647 succinimidyl ester for 1 hour at room temperature. Free dye was removed and buffer-exchanged to PBS. As measured by absorption, Fn-AF647 (denoted as pFn647) batches carried 10 to 15 dye molecules per molecule on average. For 2C STORM of pFn and F-actin, pFn was labeled with CF680 in an analog way. For micropost array detector (mPAD) experiments, BSA was labeled with DyLight 405 and adhesion proteins were labeled with Alexa Fluor 488, resulting in five to seven dyes per molecule.

Platelet isolation

Ethical approval was obtained from the Kantonale Ethikkommission Zurich (KEK-ZH-Nr. 2012-0111) and RCSI Research Ethics Committee (REC1391 and REC1504) before the commencement of the study. All experiments were performed in accordance with relevant guidelines and regulations. Whole blood from healthy adult volunteers was collected in ACD tubes. Platelets were isolated not later than 4 hours after blood withdrawal. Whole blood was centrifuged in the collection tubes at 180*g* for 15 min at room temperature. One and a half millilitres of platelet rich plasma (PRP) was collected into 2-ml tubes, 400 µl of ACD solution [dextrose 1.47% (w/v), trisodium citrate dihydrate 1.32% (w/v), and anhydrous citric acid 0.48% (w/v)] was added, and contents were gently mixed by inversion and

centrifuged at 900*g* for 5 min at room temperature. The supernatant was removed and platelet pellet was resuspended in 500 µl of prewarmed (at 37°C) Tyrode's buffer [TB; 134 mM NaCl, 12 mM NaHCO3, 2.9 mM KCl, 0.34 mM Na_2HPO_4, 1 mM $MgCl_2$, and 10 mM Hepes (pH 7.4)]. Twenty microliters of resuspended platelet pellet was added to each well in 700 µl of seeding buffer [TB containing 1.8 mM $CaCl_2$, 5 µM ADP, Fn-AF647 (10 µg/ml), and unlabeled Fn (90 µg/ml)]. Seeded platelets were incubated in the dark at 37°C for 2 hours. Next, samples were washed three times with TB and fixed with 3% paraformaldehyde (PFA) in TB for 15 min. Samples were washed three times with PBS and stored at 4°C.

For traction force measurements, the isolation protocol was slightly modified by adding prostaglandin E_1 to the PRP at final concentration 1 µM, by including apyrase (0.05 U/ml) in the wash buffer, and repeating the resuspension step another time. Platelets were counted on a hematocytometer (Sysmex). Eight million platelets were added to one 12-well chamber that contained the mPADs on a 20-mm coverslip and 800 µl of seeding buffer (TB containing 1.8 mM $CaCl_2$ and 5 µM ADP), gently mixed, and incubated at 37°C for 1 hour.

Platelets and sample preparation for STORM imaging

Fn, Ln, and Col4 were coated with a concentration of 100 µg/ml (in PBS) overnight at 4°C onto coverslips as described previously (*19*). Cross-linked Fb matrix was generated as described before (*16*) by mixing human Fg (500 µg/ml), thrombin (3 U/ml), FXIII (5 µg/ml), and $CaCl_2$ (2 mM) in 0.5 ml of tris-buffered saline [20 mM tris-HCl (pH 7.4) and 150 mM NaCl] and incubation of coverslips with this mixture overnight at 4°C. All coverslips were washed thoroughly three times with PBS before use. Isolated washed platelets were resuspended in TB [containing 1.8 mM Ca^{2+}, 5 µM ADP, unlabeled Fn (90 µg/ml), Fn-AF647 (10 µg/ml), and, where appropriate, RUC-2, BBT, or JBS5]. After seeding on coverslips for 2 hours at 37°C, platelets were rinsed with TB, fixed with 3% (w/v) PFA in TB for 15 min, and washed with PBS.

Platelet isolation from mice

Heterozygous *Myh9* mutant mice (*35*) on mixed background were purchased from Mutant Mouse Resource & Research Centers [stock number 036210-UNC (D1424N)]. An in-house generated *Itga2b*$^{-/-}$ mouse on C57BL/6J background (Biocytogen) was used. Wild-type littermates were used as controls. Female and male mice were between 6 and 12 weeks of age. Animal studies were approved by the district government of Lower Franconia, Germany (approval number 2-523). Mice were kept at a 12-hour light/12-hour dark cycle with food and water available ad libitum in the experimental area of the animal facility. We followed the latest guidelines of ARRIVE. Anesthetized mice were bled in heparin (20 U/ml, Ratiopharm) and centrifuged for 6 min at 300*g* two times to generate PRP. After supplementation of apyrase (0.02 U/ml) and 0.5 µM prostaglandin, PRP was centrifuged for 5 min at 800*g*. The obtained platelet pellet was washed with modified Tyrodes-Hepes buffer [134 mM NaCl, 0.34 mM Na_2HPO_4, 2.9 mM KCl, 12 mM $NaHCO_3$, 5 mM Hepes, 1 mM $MgCl_2$, 5 mM D-glucose, and 0.35% BSA (pH 7.4)] containing 0.5 µM prostacyclin and apyrase (0.02 U/ml). After centrifugation for 5 min at 800*g*, platelets were resuspended in Tyrodes-Hepes buffer in the presence of apyrase (0.02 U/ml) to a platelet count of 300,000 platelet/µl. Platelet suspension was incubated at 37°C for 30 min. Platelets were seeded onto coverslips in the presence of low-dose thrombin (0.01 U/ml, Roche) and processed identical to human platelets otherwise.

Confocal imaging and morphometrics

Coverslips were mounted in a chamber (Chamlide; Live Cell Instruments, South Korea) on a confocal laser scanning microscope (SP8; Leica Microsystems, Germany) using a 63× oil immersion objective and 2× zoom (resulting in a field of view of 123 µm by 123 µm at a pixel size of 60.1 nm) and excitation at 488 and 647 nm. For statistical analysis of platelet morphology and the pFn distribution, between 200 and 300 cells were recorded per condition at six to eight different field of views on the sample.

Morphometric image analysis was performed as previously described (*19*). Briefly, outlines of single platelets were automatically extracted from F-actin fluorescence images by thresholding, which yielded the single-cell spreading area.

Fabrication, optimization, and imaging of the micropost substrates

Resist-coated silicon wafers were patterned with circles (diameter, 1 µm; center-to-center spacing, 2 µm) using 220-nm deep ultraviolet (UV) lithography (ABM, USA). Then, the resists were etched with a fluorine-based inductively coupled plasma process (PlasmaPro100 Estrelas, Oxford Instruments, UK) to create 2.6-µm-deep post structures. Master structures were replicated by creating elastomeric negative molds using a sandwich of spin-coated hard PDMS and Sylgard 184 and subsequent molding using hard PDMS on glass coverslips. The spring stiffness of posts was calculated as 34.51 nN/µm (*63*). The top surface of the posts was then coated with adhesion protein (1:1 mixture of labeled/unlabeled) by contact printing after UV/ozone activation. Coating and transfer efficiencies were measured as explained in fig. S17 and were largely independent of the protein used. The remaining accessible mPAD surface was stained and passivated with fluorescent BSA (0.4 mg/ml) for 30 min and then 0.5% (w/v) Pluronics F127 for 30 min. Washed platelets from healthy volunteers were seeded for 1 hour on the washed arrays and subsequently fixed with 3% (w/v) FA in PBS for 15 min. Samples were stained with phalloidin 647, and fluorescent *z* stacks were acquired by confocal microscopy (Leica SP8 or Zeiss Examiner Z.1) at a pixel size of 60 to 70 nm. The deflection of posts was determined from the BSA channel. Briefly, positions of individual posts were determined by template matching and a radial symmetry fit. Positions of single posts were linked through slices of the *z* stack. The lateral offset between slices was determined by a redundant cross-correlation of nondeflected posts in the region around cells and corrected. The deflection profile of posts was approximated by a c-spline, yielding deflection amplitude and directions of post tops. Forces per post were calculated by Hooke's law using the spring stiffness. The median apparent force of posts in the region outside of cells was taken as the measurement resolution. The spreading area of cells was determined from outlines based on the F-actin stain. The mean force per post is the average of the force magnitudes of individual posts beneath a single cell. The total force per cell is the sum of the force magnitudes of all posts beneath a single cell not taking into account their direction.

Lattice light sheet microscopy

Fresh blood from a healthy donor was collected in ACD citrated tubes. After 5 min before incubation with 2 mM $CaCl_2$, 10 µM ADP, Fn (50 µg ml^{-1}) (10% Fn-AF-488), and Fg (50 µg ml^{-1}) (10% labeled

Fg-AF-546), the blood was incubated on Fn-coated glass coverslips (18 mm, #1.5) at 37°C on an orbital shaker (3D-300, FinePCR, South Korea) with 100 rpm for 60 min and subsequently fixed with 3% (w/v) PFA in PBS for 15 min. Coverslips were directly mounted in a magnetic chamber (Chamlide; Live Cell Instruments, South Korea) and imaged with a preserial Lattice Light Sheet 2 (Zeiss, Germany) equipped with three laser lines (488, 561, and 640 nm), a scientific complementary metal-oxide semiconductor camera (pco. edge; PCO, Germany) and a 48×/1.0 numerical aperture detection objective and the Sinc3 15 × 650 lightsheet. A field of view of 78,111 μm^2 (pixel size of 0.145 μm) and depth of 34 μm were recorded. The subsequent deconvolution and deskewing were performed with Zen Blue software (Zeiss, Germany).

STORM imaging of Fn and the cytoskeleton

During platelet seeding and spreading, the medium was supplemented with pFn647 (10 μg/ml) and unlabeled pFn (90 μg/ml) that get incorporated into the Fn fibrils assembled by platelets, as previously observed for fibroblasts. Afterward, samples were fixed and stained for the actin cytoskeleton by incubating with Alexa Fluor 488 phalloidin at 1:50 dilution for 1 hour for epifluorescence. For 2C STORM of pFn and F-actin, Alexa Fluor 647 phalloidin was used instead. For 2C STORM of pFn and vinculin, samples were incubated overnight at 4°C with 1:60 dilution of anti-vinculin antibody in 3% (w/v) BSA. Next, samples were rinsed three times in PBS and incubated for 1 hour with 1:60 dilution of anti-mouse CF680 in 3% BSA. After three washes in PBS, samples were postfixed with 4% PFA in PBS for 15 min. A home-built setup was used for single-molecule localization microscopy, as previously described (*62*). Extended *z*-range 3D STORM was performed by a looped acquisition at several *z* slices and subsequent registration of 3D single molecule data (*64*). Fitting and analysis of STORM movies were performed using experimental point-spread functions (*65*) in the software SMAP (*66*).

Analysis of fibril dimensions

Fn fibrils were analyzed as shown exemplary in fig. S1. The STORM images were postprocessed in SMAP and only *z* localizations with a localization precision better than 100 nm were further analyzed. Single fibers were manually marked from start to end by a line region of interest which defined the *x* coordinate. The length was taken as the length of the line. To distinguish Fn fibrils from Fn aggregates, only fibrils longer than 1 μm were analyzed. The diameter was defined as the full width half maximum of a Gaussian fit of the perpendicular line profile with 2-nm binning. The inclination and start-to-end height were determined by a line fit to *z* localizations binned into 20 intervals along *x*. No masking/blinding was applied during analysis. The number of fibrils that were analyzed per platelet under control conditions on Fn ranged from 1 to 5, with a mean of three fibrils per platelet. The number of fibrils per cell was not quantified for all conditions.

Analysis of the lateral offset between vinculin and Fn fibrils at fibrillar adhesion sites

Lines were drawn along fibrillar adhesion sites from inside the cell toward to outside anchorage of the Fn fibrils. Fluorophore localizations in both channels (vinculin and Fn) that were within a 150-nm-wide region around these lines were rotated to align them in the *x* direction. The start of the vinculin adhesion and of the Fn fibril was set to the 0.05 quantile of *x* positions of localizations in the respective channel. This procedure allowed for a robust determination of the signal boundaries in the presence of background localizations (fig. S15). No masking/blinding was applied during analysis.

Manual count of Fn fibrils

Fraction of platelets that assembled Fn were measured manually. At least 30 different field of views (48.1 μm by 48.1 μm) were captured in the pFn channel on the epifluorescence microscope, and platelets that assemble pFn fibrils (fibril length > 1 μm) and platelets that only deposit pFn (fibril length < 1 μm) were separately counted and the ratio was determined.

ILK S^{246} and integrin β_3 Y^{773} phosphorylation

After seeding platelets on Ln-111– or Fn-coated coverslips for 2 hours at 37°C, platelets were rinsed with TB and washed twice with ice-cold PBS. Then, platelets were lysed 20 min on the coverslip using ice-cold lysis buffer (20 mM tris, 150 mM NaCl, 1 mM EGTA, 1 mM EDTA, and 1% Triton X-100 supplemented with 1:100 phosphatase inhibitor and 1:10 protease inhibitor). Platelets were scratched and lysate was collected, homogenized, and centrifuged at 4°C. Protein concentrations were determined with a BCA protein assay kit, and cell lysates were incubated with 5× reducing sample buffer [0.3 M tris-HCl (pH 6.8), 100 mM dithiothreitol, 5% SDS, 50% glycerol, and pyronin G] for 5 min at 95°C. Equal amounts of protein were separated by SDS–polyacrylamide gel electrophoresis (4 to 20% precast polyacrylamide gels) under reducing conditions, transferred to nitrocellulose membrane, blocked for 1 hour with 5% BSA, and incubated with 1:500 anti-ILK pS^{246} or 1:500 anti-integrin β_3 pY^{773} or 1:1000 of anti–β-actin overnight followed by washing and the incubation of the appropriate HRP-conjugated secondary antibody (1:10,000) at room temperature for 1 hour. The membrane was exposed to Western blotting substrate, and the bands were visualized via chemiluminescence. The level of protein phosphorylation was quantified by ImageJ software and normalized by β-actin (loading control).

SUPPLEMENTARY MATERIALS

Supplementary material for this article is available at https://science.org/doi/10.1126/sciadv.abj8331

View/request a protocol for this paper from *Bio-protocol*.

REFERENCES AND NOTES

1. M. Rodrigues, N. Kosaric, C. A. Bonham, G. C. Gurtner, Wound healing: A cellular perspective. *Physiol. Rev.* **99**, 665–706 (2019).
2. L. H. Ting, S. Feghhi, N. Taparia, A. O. Smith, A. Karchin, E. Lim, A. S. John, X. Wang, T. Rue, N. J. White, N. J. Sniadecki, Contractile forces in platelet aggregates under microfluidic shear gradients reflect platelet inhibition and bleeding risk. *Nat. Commun.* **10**, 1204 (2019).
3. D. R. Myers, Y. Qiu, M. E. Fay, M. Tennenbaum, D. Chester, J. Cuadrado, Y. Sakurai, J. Baek, R. Tran, J. C. Ciciliano, B. Ahn, R. G. Mannino, S. T. Bunting, C. Bennett, M. Briones, A. Fernandez-Nieves, M. L. Smith, A. C. Brown, T. Sulchek, W. A. Lam, Single-platelet nanomechanics measured by high-throughput cytometry. *Nat. Mater.* **16**, 230–235 (2017).
4. P. Nurden, A. T. Nurden, Congenital disorders associated with platelet dysfunctions. *Thromb. Haemost.* **99**, 253–263 (2008).
5. L. Nicolai, K. Schiefelbein, S. Lipsky, A. Leunig, M. Hoffknecht, K. Pekayvaz, B. Raude, C. Marx, A. Ehrlich, J. Pircher, Z. Zhang, I. Saleh, A. K. Marel, A. Löf, T. Petzold, M. Lorenz, K. Stark, R. Pick, G. Rosenberger, L. Weckbach, B. Uhl, S. Xia, C. A. Reichel, B. Walzog, C. Schulz, V. Zheden, M. Bender, R. Li, S. Massberg, F. Gaertner, Vascular surveillance by haptotactic blood platelets in inflammation and infection. *Nat. Commun.* **11**, 5778 (2020).

6. A. Hielscher, K. Ellis, C. Qiu, J. Porterfield, S. Gerecht, Fibronectin deposition participates in extracellular matrix assembly and vascular morphogenesis. *PLOS ONE* **11**, e0147600 (2016).
7. M. A. Burkhardt, J. Waser, V. Milleret, I. Gerber, M. Y. Emmert, J. Foolen, S. P. Hoerstrup, F. Schlottig, V. Vogel, Synergistic interactions of blood-borne immune cells, fibroblasts and extracellular matrix drive repair in an in vitro peri-implant wound healing model. *Sci. Rep.* **6**, 21071 (2016).
8. Y. Wang, A. Reheman, C. M. Spring, J. Kalantari, A. H. Marshall, A. S. Wolberg, P. L. Gross, J. I. Weitz, M. L. Rand, D. F. Mosher, J. Freedman, H. Ni, Plasma fibronectin supports hemostasis and regulates thrombosis. *J. Clin. Invest.* **124**, 4281–4293 (2014).
9. P. Singh, C. Carraher, J. E. Schwarzbauer, Assembly of fibronectin extracellular matrix. *Annu. Rev. Cell Dev. Biol.* **26**, 397–419 (2010).
10. J. Lu, A. D. Doyle, Y. Shinsato, S. Wang, M. A. Bodendorfer, M. Zheng, K. M. Yamada, Basement membrane regulates fibronectin organization using sliding focal adhesions driven by a contractile winch. *Dev. Cell* **52**, 631–646.e4 (2020).
11. S. Fernandez-Sauze, D. Grall, B. Cseh, E. Van Obberghen-Schilling, Regulation of fibronectin matrix assembly and capillary morphogenesis in endothelial cells by Rho family GTPases. *Exp. Cell Res.* **315**, 2092–2104 (2009).
12. B. Cseh, S. Fernandez-Sauze, D. Grall, S. Schaub, E. Doma, E. Van Obberghen-Schilling, Autocrine fibronectin directs matrix assembly and crosstalk between cell-matrix and cell-cell adhesion in vascular endothelial cells. *J. Cell Sci.* **123**, 3989–3999 (2010).
13. O. E. Olorundare, O. Peyruchaud, R. M. Albrecht, D. F. Mosher, Assembly of a fibronectin matrix by adherent platelets stimulated by lysophosphatidic acid and other agonists. *Blood* **98**, 117–124 (2001).
14. J. Cho, D. F. Mosher, Characterization of fibronectin assembly by platelets adherent to adsorbed laminin-111. *J. Thromb. Haemost.* **4**, 943–951 (2006).
15. J. Cho, D. F. Mosher, Impact of fibronectin assembly on platelet thrombus formation in response to type I collagen and von Willebrand factor. *Blood* **108**, 2229–2236 (2006).
16. J. Cho, J. L. Degen, B. S. Coller, D. F. Mosher, Fibrin but not adsorbed fibrinogen supports fibronectin assembly by spread platelets. *J. Biol. Chem.* **280**, 35490–35498 (2005).
17. M. Benito-Jardón, S. Klapproth, I. Gimeno-Lluch, T. Petzold, M. Bharadwaj, D. J. Müller, G. Zuchtriegel, C. A. Reichel, M. Costell, The fibronectin synergy site re-enforces cell adhesion and mediates a crosstalk between integrin classes. *eLife* **6**, e22264 (2017).
18. T. H. Barker, A. J. Engler, The provisional matrix: Setting the stage for tissue repair outcomes. *Matrix Biol.* **60-61**, 1–4 (2017).
19. S. Lickert, S. Sorrentino, J.-D. Studt, O. Medalia, V. Vogel, I. Schoen, Morphometric analysis of spread platelets identifies integrin αIIbβ3-specific contractile phenotype. *Sci. Rep.* **8**, 5428 (2018).
20. C. A. Lemmon, C. S. Chen, L. H. Romer, Cell traction forces direct fibronectin matrix assembly. *Biophys. J.* **96**, 729–738 (2009).
21. Y. Schurr, A. Sperr, J. Volz, S. Beck, L. Reil, C. Kusch, P. Eiring, S. Bryson, M. Sauer, B. Nieswandt, L. Machesky, M. Bender, Platelet lamellipodium formation is not required for thrombus formation and stability. *Blood* **134**, 2318–2329 (2019).
22. J. Liu, Y. Wang, W. I. Goh, H. Goh, M. A. Baird, S. Ruehland, S. Teo, N. Bate, D. R. Critchley, M. W. Davidson, P. Kanchanawong, Talin determines the nanoscale architecture of focal adhesions. *Proc. Natl. Acad. Sci. U.S.A.* **112**, E4864–E4873 (2015).
23. D. Chada, T. Mather, M. U. Nollert, The synergy site of fibronectin is required for strong interaction with the platelet integrin αIIbβ3. *Ann. Biomed. Eng.* **34**, 1542–1552 (2006).
24. M. Zeiler, M. Moser, M. Mann, Copy number analysis of the murine platelet proteome spanning the complete abundance range. *Mol. Cell. Proteomics* **13**, 3435–3445 (2014).
25. J. M. Burkhart, M. Vaudel, S. Gambaryan, S. Radau, U. Walter, L. Martens, J. Geiger, A. Sickmann, R. P. Zahedi, P. Zahedi, J. Geiger, A. Sickmann, R. P. Zahedi, The first comprehensive and quantitative analysis of human platelet protein composition allows the comparative analysis of structural and functional pathways. *Blood* **120**, e73–e82 (2012).
26. F. Stanchi, C. Grashoff, C. F. N. Yonga, D. Grall, R. Fässler, E. Van Obberghen-Schilling, Molecular dissection of the ILK-PINCH-parvin triad reveals a fundamental role for the ILK kinase domain in the late stages of focal-adhesion maturation. *J. Cell Sci.* **122**, 1800–1811 (2009).
27. N. Elad, T. Volberg, I. Patla, V. Hirschfeld-Warneken, C. Grashoff, J. P. Spatz, R. Fässler, B. Geiger, O. Medalia, The role of integrin-linked kinase in the molecular architecture of focal adhesions. *J. Cell Sci.* **126**, 4099–4107 (2013).
28. K. R. Legate, R. Fassler, Mechanisms that regulate adaptor binding to beta-integrin cytoplasmic tails. *J. Cell Sci.* **122**, 187–198 (2009).
29. P. Atherton, B. Stutchbury, D. Jethwa, C. Ballestrem, Mechanosensitive components of integrin adhesions: Role of vinculin. *Exp. Cell Res.* **343**, 21–27 (2016).
30. B. Suki, H. Parameswaran, J. Imsirovic, E. Bartolák-Suki, Regulatory roles of fluctuation-driven mechanotransduction in cell function. *Phys. Ther.* **31**, 346–358 (2016).
31. E. Zamir, M. Katz, Y. Posen, N. Erez, K. M. Yamada, B.-Z. Katz, S. Lin, D. C. Lin, A. Bershadsky, Z. Kam, B. Geiger, Dynamics and segregation of cell–matrix adhesions in cultured fibroblasts. *Nat. Cell Biol.* **2**, 191–196 (2000).
32. F. Margadant, L. L. Chew, X. Hu, H. Yu, N. Bate, X. Zhang, M. Sheetz, Mechanotransduction in vivo by repeated talin stretch-relaxation events depends upon vinculin. *PLOS Biol.* **9**, e1001223 (2011).
33. W. A. Lam, O. Chaudhuri, A. Crow, K. D. Webster, T.-D. Li, A. Kita, J. Huang, D. A. Fletcher, Mechanics and contraction dynamics of single platelets and implications for clot stiffening. *Nat. Mater.* **10**, 61–66 (2011).
34. A. Yoneda, D. Ushakov, H. A. B. Multhaupt, J. R. Couchman, Fibronectin matrix assembly requires distinct contributions from Rho kinases I and -II. *Mol. Biol. Cell* **18**, 66–75 (2007).
35. Y. Zhang, M. A. Conti, D. Malide, F. Dong, A. Wang, Y. A. Shmist, C. Liu, P. Zerfas, M. P. Daniels, C.-C. Chan, E. Kozin, B. Kachar, M. J. Kelley, J. B. Kopp, R. S. Adelstein, Mouse models of MYH9-related disease: Mutations in nonmuscle myosin II-A. *Blood* **119**, 238–250 (2012).
36. J. Baumann, L. Sachs, O. Oliver, I. Schoen, P. Nestler, C. Zaninetti, M. Kenny, R. Kranz, H. von Eysmondt, J. Rodriguez, T. E. Schäffer, Z. Nagy, A. Greinacher, R. Palankar, M. Bender, Reduced platelet forces underlie impaired hemostasis in mouse models of *MYH9*-related disease. *bioRxiv* , 2021.11.10.468045 (2021).
37. O. V. Kim, R. I. Litvinov, M. S. Alber, J. W. Weisel, Quantitative structural mechanobiology of platelet-driven blood clot contraction. *Nat. Commun.* **8**, 1274 (2017).
38. B.-Z. Katz, E. Zamir, A. Bershadsky, Z. Kam, K. M. Yamada, B. Geiger, Physical state of the extracellular matrix regulates the structure and molecular composition of cell-matrix adhesions. *Mol. Biol. Cell* **11**, 1047–1060 (2000).
39. J. Z. Kechagia, J. Ivaska, P. Roca-Cusachs, Integrins as biomechanical sensors of the microenvironment. *Nat. Rev. Mol. Cell Biol.* **20**, 457–473 (2019).
40. T. N. Durrant, M. T. Van Den Bosch, I. Hers, Integrin $\alpha_{IIb}\beta_3$ outside-in signaling. *Blood* **130**, 1607–1619 (2017).
41. V. Vouret-Craviari, E. Boulter, D. Grall, C. Matthews, E. Van Obberghen-Schilling, ILK is required for the assembly of matrix-forming adhesions and capillary morphogenesis in endothelial cells. *J. Cell Sci.* **117**, 4559–4569 (2004).
42. D. Gagné, Y. D. Benoit, J.-F. Groulx, P. H. Vachon, J.-F. Beaulieu, ILK supports RhoA/ROCK-mediated contractility of human intestinal epithelial crypt cells by inducing the fibrillogenesis of endogenous soluble fibronectin during the spreading process. *BMC Mol. Cell Biol.* **21**, 14 (2020).
43. M. Leiss, K. Beckmann, A. Girós, M. Costell, R. Fässler, The role of integrin binding sites in fibronectin matrix assembly in vivo. *Curr. Opin. Cell Biol.* **20**, 502–507 (2008).
44. F. Ye, A. K. Snider, M. H. Ginsberg, Talin and kindlin: The one-two punch in integrin activation. *Front. Med.* **8**, 6–16 (2014).
45. N. L. Malinin, L. Zhang, J. Choi, A. Ciocea, O. Razorenova, Y.-Q. Ma, E. A. Podrez, M. Tosi, D. P. Lennon, A. I. Caplan, S. B. Shurin, E. F. Plow, T. V. Byzova, A point mutation in KINDLIN3 ablates activation of three integrin subfamilies in humans. *Nat. Med.* **15**, 313–318 (2009).
46. J. M. Stevens, P. A. Jordan, T. Sage, J. M. Gibbins, The regulation of integrin-linked kinase in human platelets: Evidence for involvement in the regulation of integrin $\alpha_2\beta_1$. *J. Thromb. Haemost.* **2**, 1443–1452 (2004).
47. K. L. Tucker, T. Sage, J. M. Stevens, P. A. Jordan, S. Jones, N. E. Barrett, R. St-Arnaud, J. Frampton, S. Dedhar, J. M. Gibbins, A dual role for integrin-linked kinase in platelets: Regulating integrin function and α-granule secretion. *Blood* **112**, 4523–4531 (2008).
48. J.-M. Pasquet, M. Noury, A. Nurden, Evidence that the platelet integrin alphallb beta3 is regulated by the integrin-linked kinase, ILK, in a PI3-kinase dependent pathway. *Thromb. Haemost.* **88**, 115–122 (2002).
49. S. Honda, H. Shirotani-Ikejima, S. Tadokoro, Y. Tomiyama, T. Miyata, The integrin-linked kinase-PINCH-parvin complex supports integrin αIIbβ3 activation. *PLOS ONE* **8**, e85498 (2013).
50. C. Wu, Roles of integrins in fibronectin matrix assembly. *Histol. Histopathol.* **12**, 233–240 (1997).
51. N. J. Anthis, K. L. Wegener, D. R. Critchley, I. D. Campbell, Structural diversity in integrin/talin interactions. *Structure* **18**, 1654–1666 (2010).
52. D. A. Calderwood, V. Tai, G. Di Paolo, P. De Camilli, M. H. Ginsberg, Competition for talin results in trans-dominant inhibition of integrin activation. *J. Biol. Chem.* **279**, 28889–28895 (2004).
53. M. Riederer, M. Ginsberg, B. Steiner, Blockade of platelet GPIIB-IIIA (Integrin αIIbβ3) in flowing human blood leads to passivation of prothrombotic surfaces. *Thromb. Haemost.* **88**, 858–864 (2002).
54. C. J. McCleverty, D. C. Lin, R. C. Liddington, Structure of the PTB domain of tensin1 and a model for its recruitment to fibrillar adhesions. *Protein Sci.* **16**, 1223–1229 (2007).
55. M. Bharadwaj, N. Strohmeyer, G. P. Colo, J. Helenius, N. Beerenwinkel, H. B. Schiller, R. Fässler, D. J. Müller, αV-class integrins exert dual roles on α5β1 integrins to strengthen adhesion to fibronectin. *Nat. Commun.* **8**, 14348 (2017).
56. M. Jiroušková, J. K. Jaiswal, B. S. Coller, Ligand density dramatically affects integrin αIIbβ3-mediated platelet signaling and spreading. *Blood* **109**, 5260–5269 (2007).
57. M. Tomaiuolo, C. N. Matzko, I. Poventud-Fuentes, J. W. Weisel, L. F. Brass, T. J. Stalker, Interrelationships between structure and function during the hemostatic response to injury. *Proc. Natl. Acad. Sci. U.S.A.* **116**, 2243–2252 (2019).

58. D. Y. Nechipurenko, N. Receveur, A. O. Yakimenko, T. O. Shepelyuk, A. A. Yakusheva, R. R. Kerimov, S. I. Obydennyy, A. Eckly, C. Léon, C. Gachet, E. L. Grishchuk, F. I. Ataullakhanov, P. H. Mangin, M. A. Panteleev, Clot contraction drives the translocation of procoagulant platelets to thrombus surface. *Arterioscler. Thromb. Vasc. Biol.* **39**, 37–47 (2019).
59. L. F. Brass, S. L. Diamond, T. J. Stalker, Platelets and hemostasis: A new perspective on an old subject. *Blood Adv.* **1**, 5–9 (2016).
60. C. E. Hansen, Y. Qiu, O. J. T. McCarty, W. A. Lam, Platelet mechanotransduction. *Annu. Rev. Biomed. Eng.* **20**, 253–275 (2018).
61. Y. Zhang, Y. Qiu, A. T. Blanchard, Y. Chang, J. M. Brockman, V. P.-Y. Ma, W. A. Lam, K. Salaita, Platelet integrins exhibit anisotropic mechanosensing and harness piconewton forces to mediate platelet aggregation. *Proc. Natl. Acad. Sci. U.S.A.* **115**, 325–330 (2018).
62. S. M. Früh, I. Schoen, J. Ries, V. Vogel, Molecular architecture of native fibronectin fibrils. *Nat. Commun.* **6**, 7275 (2015).
63. I. Schoen, W. Hu, E. Klotzsch, V. Vogel, Probing cellular traction forces by micropillar arrays: Contribution of substrate warping to pillar deflection. *Nano Lett.* **10**, 1823–1830 (2010).
64. R. Diekmann, M. Kahnwald, A. Schoenit, J. Deschamps, U. Matti, J. Ries, Optimizing imaging speed and excitation intensity for single-molecule localization microscopy. *Nat. Methods* **17**, 909–912 (2020).
65. Y. Li, M. Mund, P. Hoess, J. Deschamps, U. Matti, B. Nijmeijer, V. J. Sabinina, J. Ellenberg, I. Schoen, J. Ries, Real-time 3D single-molecule localization using experimental point spread functions. *Nat. Methods* **15**, 367–369 (2018).
66. J. Ries, SMAP: A modular super-resolution microscopy analysis platform for SMLM data. *Nat. Methods* **17**, 870–872 (2020).

Acknowledgments: We thank B. S. Coller for providing the RUC compounds (RU MTA #2021-0200). We would like to acknowledge L. Braun for helpful discussions during the manuscript preparation. **Funding:** This work was financially supported by ETH Zurich, by Swiss TransMed "Life Matrix" 33/2013 (to V.V.), Wyss Zurich (to V.V.), the Velux Stiftung (to K.S.), by TR240 grant with project number 374031971 of the Deutsche Forschungsgemeinschaft (DFG; German Research Foundation) to M.B. and B.N., by Science Foundation Ireland under grant number 19/FFP/6708 (to I.S.), by RCSI (to I.S.), and by European Union's Horizon 2020 research and innovation programme under grant agreement no. 747586 (to I.S.). **Author contributions:** S.L., I.S., and V.V. laid out the major concepts of the study. M.A.B. performed initial fibrillogenesis experiments with platelets. S.L. and I.S. planned experiments. M.B. prepared washed murine platelets and, together with S.L., performed fibrillogenesis assays. B.N. oversaw the generation of *Itga2b*$^{-/-}$ mice. S.L., K.S., and M.K. performed all platelet spreading experiments. S.L. and S.M.F. performed cell culture experiments with fibroblasts. S.L. and M.K. with help of K.S. and J.L.M. performed superresolution imaging for platelets. S.M.F. performed superresolution imaging of fibroblasts. S.L. and I.S. wrote the script for fibril analysis and analyzed all superresolution data. S.L. fabricated the micropillar masters. S.L., M.K., and I.S. fabricated and optimized the micropillar arrays. S.L. and M.K. performed, imaged, and analyzed platelet traction force experiments. I.S. wrote the script for the traction force analysis. S.L., I.S., and V.V. wrote the manuscript. All authors critically revised the report. **Competing interest:** The authors declare that they have no competing interests. **Data and materials availability:** All data needed to evaluate the conclusions in the paper are present in the paper and/or the Supplementary Materials. The raw data can be provided by the authors pending scientific review. Requests for the raw data should be submitted to: ingmarschoen@rcsi.ie. RUC inhibitor materials were obtained via a material transfer agreement with Rockefeller University.

Submitted 7 June 2021
Accepted 21 January 2022
Published 11 March 2022
10.1126/sciadv.abj8331

ScienceAdvances

Platelets drive fibronectin fibrillogenesis using integrin #IIb#3

Sebastian LickertMartin KennyKateryna SelcukJohanna L. MehlMarkus BenderSusanna M. FrühMelanie A. BurkhardtJan-Dirk StudtBernhard NieswandtIngmar SchoenViola Vogel

Sci. Adv., 8 (10), eabj8331. • DOI: 10.1126/sciadv.abj8331

Science Advances (ISSN) is published by the American Association for the Advancement of Science. 1200 New York Avenue NW, Washington, DC 20005. The title *Science Advances* is a registered trademark of AAAS.